ANALYSIS OF THE IMPACT OF FORCED PITCHING OSCILLATIONS IN TRANSONIC FLOW ON THE TRANSITION ONSET AND THE AEROELASTIC BEHAVIOUR OF AN AIRFOIL

I. Cafarelli [1], C. Liauzun [1], F. Mery [2], J. Methel [2], M. Forte [2], A. Lepage [1]

[1] DAAA, ONERA, Institut Polytechnique de Paris, 92320 Châtillon, France
[2] ONERA/DMPE, Université de Toulouse, 2 avenue Edouard Belin 31055 Toulouse, France

italo.cafarelli@onera.fr   cedric.liauzun@onera.fr   arnaud.lepage@onera.fr
fabien.mery@onera.fr   jeanne.methel@onera.fr   maxime.forte@onera.fr

Abstract: Within the European Clean Sky 2 Airframe ITD/NACOR project, a 2D airfoil laminar model was designed, manufactured, highly instrumented and tested in the Onera S2MA transonic wind tunnel in order to study the behaviour of the laminar-turbulent transition on the model under either steady angles of attack or forced dynamic pitch oscillations. The instrumentation included amongst others, static pressure taps, unsteady pressure sensors, accelerometers, optical displacement sensors and a high density hot films sensor array. The hot films were calibrated in order to get the time dependent wall shear stresses on the suction surface. Several key parameters were checked such as the inflow Mach number (from M=0.5 to M=0.77), the pitch angle (steady mean angle ranging from -3° to 3°, dynamic magnitude), the oscillation frequency and the Reynolds number. Steady and unsteady analysis pertaining to the influence of the different parameters are reported, including the pressure chordwise distributions with the inferred global loads and the transition locations. The comparisons between free laminar transition configurations and fully triggered turbulent flows are also given. Besides, several (U)RANS simulations performed with the Onera CFD code elsA using a transition model based on the AHD criteria and the Spalart-Allmaras turbulence model are shown.

1   INTRODUCTION

Drag reduction has always been the primary focus of aircraft manufacturers. In the early 40s, extended laminarity was identified as an efficient way to achieve this goal. Nevertheless, it was less studied due to the difficulties to manufacture wings with extended laminar flows around them. Current technology now overcomes these difficulties by mean of passive ways (natural transition) or of flow control (hybrid laminar flow). Furthermore, the ever-growing need to decrease significantly the environmental footprint brings an additional motivation to investigate this kind of wings. Indeed, a renewed interest for them is growing rapidly within the aeronautical

community. But such "laminar wings" whose airfoil are designed for extended laminarity often have characteristics as low sweep angle and high aspect ratio, which are potentially favorable to high structural flexibility and thereby to aeroelastic instabilities. On the other hand, the boundary layer is modified when the flow around the wing is laminar on a larger part of the wing surface, thus changing the effective airfoil thickness and then the aerodynamic loads. The aeroelastic behavior is thereby modified. Furthermore, the aerodynamic behavior is unconventional as non-linearities occur at low incidences and high subsonic and transonic flight speeds, when compared to conventional wings around which the flow is fully turbulent. There is then a need to develop specific numerical tools which can be able to predict the aeroelastic behavior of laminar wings as stated by Tichy et-al [1].

Mai et-al [2] and Hebler et-al [3] have indeed shown from wind tunnel tests a specific influence of the natural transition on both steady and unsteady lift and moment evolutions of a supercritical laminar airfoil (CAST10-2) in transonic flows at a Reynolds number of about 2.10^6. Hebler [4] also showed experimentally a significant influence of the transition on the flutter stability of a 2 dofs model representing the latter airfoil. Braune et al [5] analyzed the nature of the flutter, 1 DOF or 2 DOF flutter, occurring especially close to the transonic dip of the same airfoil model, highlighting the influence of the transition on it. Braune et-al [6] carried out experimental investigations on the mechanisms yielding the aerodynamic resonance and the 1 DOF LCO observed with the CAST10-2 airfoil for transonic aerodynamic conditions. Mai et-al [7] performed experiments to investigate the steady and unsteady flows around another supercritical laminar airfoil (NLF-0415) to which harmonic motions were applied, at higher Reynolds numbers, up to 14.10^6, and at lower Mach numbers, about 0.3. Lepage et al [8] investigated the impact of the transition on the aerodynamic response of a high sweep angle wing in low speed flows, by applying harmonic pitching motions to the wing. Crossflow transition was found to be triggered by the sweep angle.

All these authors exhibited a steady and unsteady aerodynamic behavior and an aeroelastic one specific to the laminar wings with a significant impact of the transition. Poirel et-al [9],[10] showed an interaction between the transition and the pitching mode of a wind tunnel model of the NACA12 airfoil at transitional Reynolds number. Aeroelasticity for the laminar wings has then to be considered with care, and specific models which can take into account the laminar to turbulent transition have to be built.

On one hand, CFD RANS based methods have proven to be suitable for aeroelastic high fidelity simulations of conventional transonic airplanes, especially to predict the flight shape and thus the aerodynamic performance [11], the load and gust responses [12]-[15], and the aeroelastic stability of conventional airplanes [11],[16] for a wide range of flight conditions. Garrigues presented the use of high fidelity numerical simulations for aeroelasticity in Dassault Aviation in [17]. Nowadays (U)RANS modelling seems to be the best compromise between the computational time and the requested accuracy for non-linear aeroelasticity. On the other hand, CFD RANS based methods associated with specific models or criteria which handle the transition have also proven to be efficient for the prediction of steady aerodynamics [18]. Several ways of modelling the transition within a RANS simulation have been proposed. The intermittency variable is added to the conservative and turbulent variables and acts as a weighting function of the turbulent quantities (turbulent viscosity or Reynolds stress tensor for examples). It can vary from 0 for laminar areas to 1 for turbulent areas. Criteria based on local or non local data, and models based on transport equations have been developed to predict natural transition according to its nature (Tollmien-

Schlichting instabilities, cross flow instability, attachment line transition, bypass transition…). Such criteria or models yield most of the time the values of the intermittency variable. A first family of transition models gathers numerous criteria using local or non-local data, which are used to determine if the flow at the investigated position is laminar or turbulent. Local means here that the knowledge of boundary layer quantities is required only at the investigated position. Such criteria provide most of the time the value of a critical Reynolds number from empirical correlations between boundary layers quantities and the external turbulence level [19]-[21]. Non local transition criteria, i.e. criteria which take into account the boundary layer history, have also been developed taking into account the nature of the transition. The AHD (Arnal-Habiballah-Delcourt) criterion [22]-[23], based on the systematic linear stability theory, is used to model the transition induced by Tollmien-Schlichting instabilities. Separation induced transition is modelled by Gleyzes [24] and Roberts [25] criteria and crossflow transition is accounted for by C1 criterion [26]. A second family of transition models is made of correlation-based models compatible with modern CFD techniques usable for complex geometries. Such models derive the intermittency variable from algebraic function relying on local flow data, as proposed by Cakmakcioglu [27], or from transport equations. The intermittency is then applied to the production terms of the turbulence models. The most popular are the models proposed by Langtry and Menter, in which two additional transport equations, one for the intermittency and one for a transition onset criterion based on momentum-thickness Reynolds number are solved [28]. More recently, Fehrs proposed a one equation model to improve transition prediction for low external turbulence and high Reynolds Number flows [29]. A new approach for the transition modelling is emerging and consists in developing transport equations formulations of stability-based semi-empirical criteria [30]-[31]. A last way of taking into account transition consists in coupling inviscid flow solvers with a boundary layer one as shown by Bargin et-al who worked on the design of an innovative laminar wing using this technique [32].

But such transition numerical models have been slightly assessed for the prediction of the unsteady aerodynamics implied by aeroelastic phenomena, especially flutter instabilities or LCO. Fehrs [33] and Fehrs et-al [34] first assessed the γ-Re_θ transition model implemented in the DLR TAU code on the CAST10-2 airfoil for high subsonic and transonic flows. The static non-linear behavior of the lift and drag coefficient characterized by the laminar drag bucket which was observed experimentally [3] was well reproduced. They carried out flutter investigations with a 2-dof structure and noticed a different behavior with a sharper transonic dip occurring at lower Mach numbers with transitional flows. Fehrs et-al [35] pursued the latter investigations: they evaluated the "γ" transition model by comparing their results with the γ-Re_θ model, the e^N method and experimental data for several airfoils and operating conditions. An analysis of the impact of the transition unsteadiness on the aerodynamic response to pitching oscillations of the airfoils was carried out by Fehrs-al [36] who noticed that the impact is higher for transonic flows with shocks. The specific behaviors of the CAST10-2 airfoil observed from wind tunnel tests [2]-[4], i.e. the static drag bucket and the unsteady aerodynamic resonance, were also well reproduced by using high order ILES simulations, thus without any specific transition model [37], and by using inviscid – boundary layer coupling computations [38]. The steady drag bucket phenomenon was also observed for a laminar supercritical airfoil designed by Dassault Aviation and for which wind tunnel tests were performed for high subsonic and transonic flow conditions within the framework of the European funded project CLEANSKY/SFWA. Liauzun et-al [39] performed simulations for this case using 3 techniques: RANS with both the γ-Re_θ model and the AHD criteria implementations in the Onera CFD code elsA (property of Airbus, Safran and Onera) [40], and a

viscous_inviscid coupling formulation developed by Le Balleur [41]. The drag bucket was numerically well reproduced using the viscous-inviscid coupling technique and the RANS model with the AHD criterion but not using the γ-Re_θ model.

Although some authors have conducted studies about the aeroelasticity of laminar wings, there is still very few data about it, especially regarding the aerodynamic response of wings to harmonic motions. Because this step remains essential to understand the aeroelastic behavior of this kind of wing, wind tunnel tests were planned within the framework of the European funded project CLEAN SKY 2/NACOR in order to investigate the unsteady aerodynamics and the laminar to turbulent transition behaviour of a symmetrical laminar airfoil under applied pitching motions. This paper presents an extensive overview of the wind tunnels tests and the related experimental and numerical analyses. The influence of different key parameters and the comparison between a natural laminar flow and a fully turbulent one will be examined.

2   EXPERIMENTAL SETUP

2.1   Model description and implementation in wind tunnel facility

The experiments were performed in the transonic guided test section of the Onera S2MA wind tunnel with height x width dimensions 1.77m * 1.75 m (see Figure 1).

The STUNTT program (Surface imperfecTion and UNsteady moTion impact on Transition onset) developed by Onera within this Clean Sky 2's Airframe ITD/NACOR project focused on joint tests with 2 models :

-   a 1st static model aiming at studying a range of default imperfections on a laminar profile [42] ;
-   a 2nd dynamic model used for investigating the unsteady behaviour of the laminar-turbulent transition mainly in transonic conditions under forced dynamic pitch oscillations which is the subject of this paper.

The peculiarity of both models was restricted to their central part while the outer parts and the relating hardware was shared by both models. Hence, these latter exhibited the same geometric characteristics and were driven by the same hydraulic system. More precisely, the 2nd model is made of 2 parts:

-   the central one (wing section) is mainly built with composite skins for high stiffness and weight lightness reasons. It contains the steady and unsteady instrumentation.
-   the 2 outer stubs are made of metal and are attached to the hydraulic pitch driving set-up; this latter includes symmetrically on each side of the model a hydraulic rotating jack combined with an electro-hydraulic servovalve and a thrust bearing, see Figure 2. The axis of rotation is aligned with the quarter chord of the model.

The overall span of the model is equal to 1.75m so as to fit the wall-to-wall test section width, with a constant chord length of 0.4m.

In order to lessen potential acoustic disturbances, the usually perforated floor and ceiling of the wind tunnel test section were both taped. The turbulence intensity was checked for Mach numbers up to 0.8 and for frequencies ranging from 3Hz to 20 KHz: the maximum turbulence level thus measured remained less than 0.2%. [42].

Figure 1: STUNTT model mounted in the S2MA ONERA wind tunnel
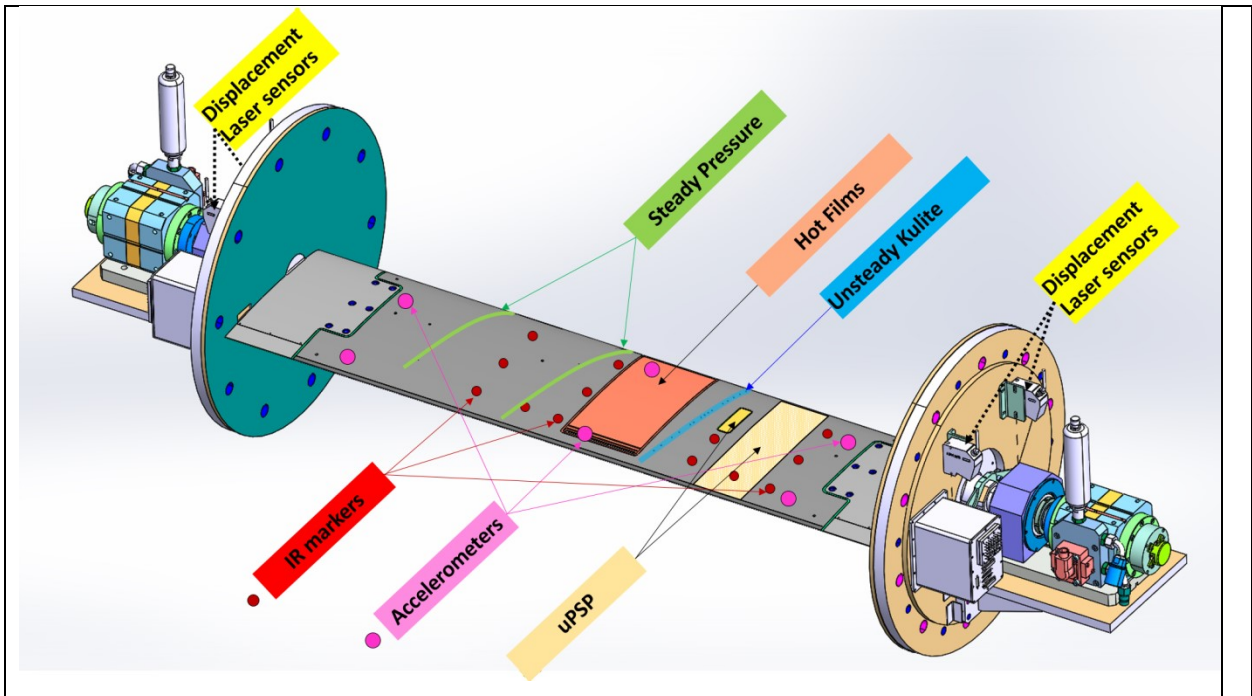

Figure 2: CAD of the whole model with instrumentation

2.2 Model instrumentation

The model airfoil, although different from supercritical ones recalled in the introduction, is representative of a laminar nacelle section developed by Onera during a previous research project. It is based on a symmetrical profile whose relative thickness is equal to 8.5%.

Figure 3 displays a sketch of the model recalling the overall used instrumentation and the optical metrologies:

- Unsteady pressure sensors: mainly Kulite type XCQ 093D; 22 on the upper face; 10 on the lower face. The upper distribution was fitted in order to line up with the hot films locations.
- Static pressure taps: 1 row centered on the mid-span of the model, composed of 42 taps on the suction side and 22 on the pressure side; 1 row at 25% left span composed of 21 taps on the upper side and 20 taps on the lower side.
- Accelerometers: 6 accelerometers distributed in the LE section and the TE section in order to have an insight on the exact dynamic angular position of the model and to monitor its dynamic behavior (either during lab tests preparation or wind tunnel tests).
- Laser displacement sensors: 4 Keyence type located by pairs on the outer parts of the model, as close as possible to the starboard and port side stubs. Each set of 2 sensors is aiming at a reference target bar linked to the model axis of rotation and thus allows to infer in real time the angular position (static and dynamic) of the model. The resulting angular error of linearity is less than 0.004°.
- Infrared Markers: 13 targets located on the upper surface of the model in order to measure the transition onset.
- Unsteady PSP (uPSP): 2 surfaces implemented on the upper surface of the model with different methods of applying the painting.
- Hot films: a 43 sensor array of type Senflex® manufactured by TAO Systems (USA) and spread on a customized sheet on the upper central section of the model, with a 10° sweep angle with respect to the flow direction in order to avoid potential thermal upstream disturbances. In order to get the hot films flush mounted, the sheet (about 330 mm by 200mm) was glued in a recess with slightly larger dimensions but equal thickness. The electron beam deposited nickel sensors elements are approximately 1.45mm long, 0.1mm wide and 0.2μm thick. They are distributed from 5% chord to 80% chord with a stream-wise spacing varying from 2.5% chord (leading edge region, x/c < 25% chord) to 3% chord (x/c > 70% chord) and 1.5% chord otherwise. The electrical connections are located inside the model, at the back of the substrate, enabling the wirings to route inside the airfoil towards both span end stubs.

The comparison of both lines of static taps pressure for the different configurations tested exhibited a good similarity, bearing out the two-dimensional flow hypothesis; hence it is assumed that the full instrumentation, since located within 25% from the centerline of either spanwise side, is subjected to the same flow conditions with no interference of the walls.

The hot films were calibrated in laboratory using calibrated probes in order to get the true local wall shear stress in the boundary layer of the model.
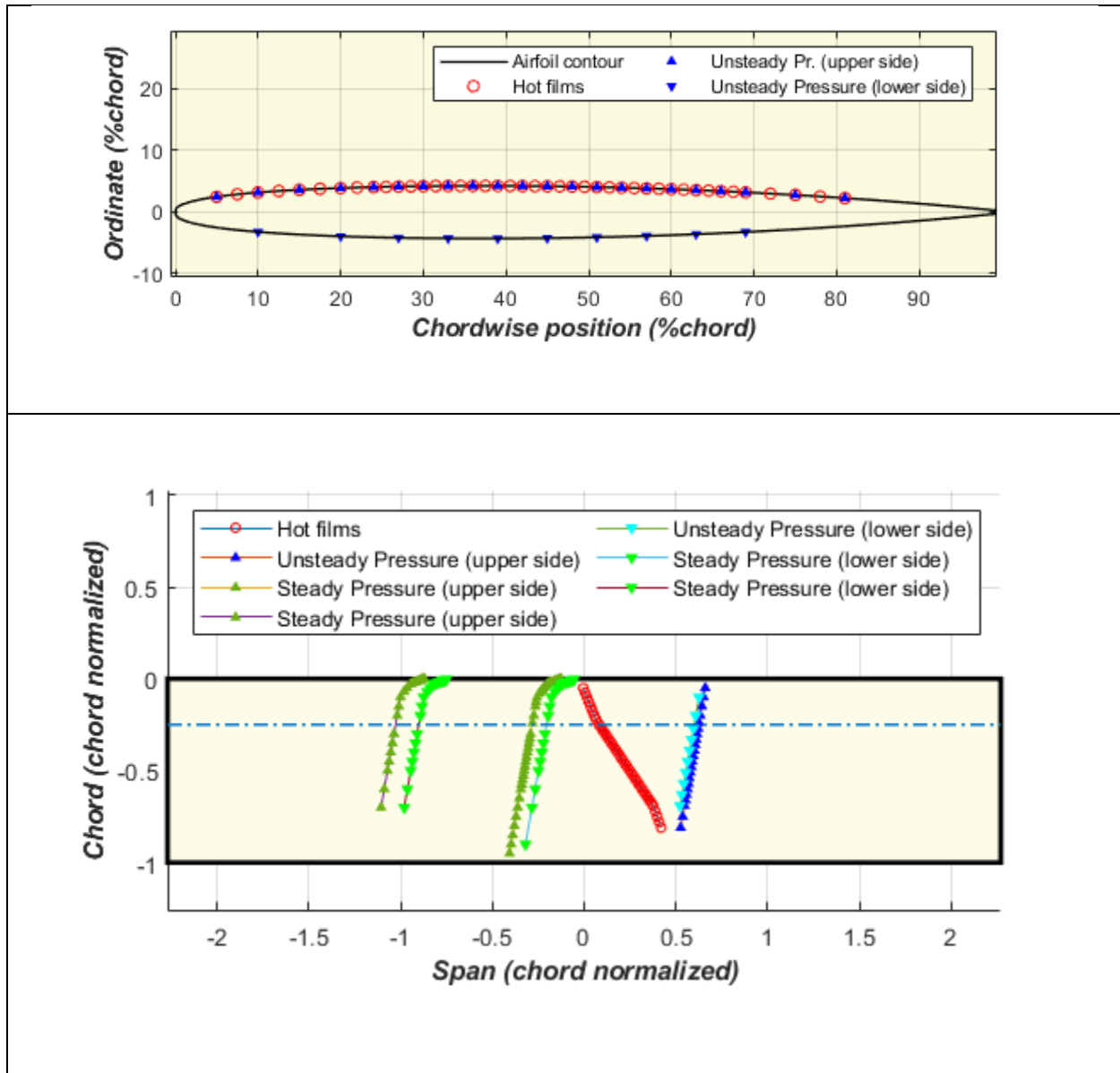
Figure 3: Schematic of model instrumentation distribution: (upper) airfoil section ; (lower) planform section.

2.3   Wind tunnel tests

Four types of tests were done:

- stabilized steady points (named SS) corresponding to fixed pitch angles of the model;
- stabilized dynamic points (named SD) corresponding to dynamic variations of the pitch amplitude around a fixed mean value;
- quasi-steady polars carried out by increasing slowly the pitch angle of the model from about -3° to 3°. As the duration of such test points was set to 180s, the resulting pitch rate amounts to about 0.03°/s validating ergo the quasi-steady assumption.

-   dynamic polars defined by increasing slowly the mean pitch angle of the model while simultaneously imposing a dynamic oscillation at a fixed frequency and a fixed dynamic amplitude.

The main corresponding parameters investigated and their overall ranges are listed below:

-   The freestream velocity was varied from Mach number M=0.5 to M=0.8 including a subsonic configuration (M=0.5), a high subsonic configuration (M=0.68) and the transonic configuration (M=0.77-0.8).
-   The stagnation pressure Pi was set at 0.6 bar for major tests. A Reynolds sensitivity at transonic Mach numbers was performed by varying the pressure from 0.6 bar to 1 bar ; the corresponding Reynolds numbers based on the airfoil chord Re_c was thus ranging at M=0.8 from $2.8 10^6$ to $5 10^6$.
-   The steady angles of attack of the model were contained between -3° and 3°.
-   The dynamic amplitude of the pitch oscillations about the quarter-chord were set at a maximum angle of 0.5°; highers values up to 2° were tested only in some subsonic configurations.
-   The pitch oscillation frequencies were changed from 0 to almost 54 Hz resulting in chord length based reduced frequencies ω_r ($\omega_r = \omega * chord / V$) varying from 0 to almost 0.5.

Besides , for all the above parameters, two overall transition configurations were simulated :

-   a 1st one named NLF (natural laminar flow) where the free transition would occur in a "natural" way;
-   a 2nd one named TRIG (with an artificially triggered turbulence) where triggering was set by sticking full span CAD-CUT® strips with 0.127 mm dots high at 5% of chord on both upper and lower surfaces.

2.4   Steady and unsteady data acquisition

Steady pressures were acquired by the wind tunnel measurement chain at a low sampling frequency of about 4 Hz.

All the other sensors (unsteady pressure sensors, hot films, accelerometers, optical displacements sensors) were acquired using an unsteady Simcenter SCADAS Lab (Siemens) data acquisition hardware based on 24 bit delta-sigma analog to digital converters. A maximum available bandwidth was set by imposing a sampling frequency of 51.2 KHz for all channels in order to handle high frequency phenomena.

The acquisition duration of each test point (stabilized steady pitch or stabilized dynamic pitch), was set to about 30s. For polar runs, the duration of the overall test point was set to 180s.

Lastly, before and after each test run series, the acquisition of the whole instrumentation was performed and is used for setting "clean" zero conditions during the post processing.

3   NUMERICAL METHOD AND COMPUTATIONAL IMPLEMENTATION

Numerical simulations were performed to be compared with the experimental data. They were carried out by using CFD techniques to solve the (U)RANS equations associated with the Spalart-Allmaras turbulence model and the AHD transition model. The term "AHD criteria" refers to an

association of the Arnal-Habiballah-Delcourt criterion which is based on the systematic linear stability theory and detects the transition due to the Tollmien-Schlichting waves instability [22] [23] and the Roberts [25] and Gleyzes [24] criteria which handle the transition due to flow separations. The AHD criteria provide the intermittency coefficient γ whose values range from 0 for laminar flows to 1 for fully turbulent flows. This coefficient is applied to compute the effective dynamic viscosity μ used in the momentum and energy conservation equations: $\mu = \mu_{lam} + \gamma\mu_{tur}$ where the laminar dynamic viscosity μ_{lam} is derived from the Sutherland law and the turbulent one μ_{tur} is provided by the turbulence model. The-assessment of the location of the intermittency region is in that case straightforward (region where γ grows from 0 to 1). This AHD model is based on the assumption that streamlines at the boundary layer edge follow the mesh lines and that the stagnation point is known. The more recent model based on a formulation of the AHD criteria using 4 additional transport equations [30] **Erreur ! Source du renvoi introuvable.**associated with the Menter k-ω SST turbulence model is also assessed. Those transition models were compared with the more popular Menter-Langtry $\gamma-Re_\theta$ model [28] and with the ISES approach based on viscous-inviscid coupling [21] [43].

The numerical simulations were performed using the elsA code (joint property of SAFRAN and ONERA) [40]. The latter is a structured finite volume cell-centered code in which numerous space and time discretization schemes are implemented. A Jameson centered space scheme was used for this study.

A structured C-mesh was built around the airfoil with far-field boundaries located 80 chords away, 360 cells on the airfoil walls with a maximum size of 0.78% of chord and 220 cells from the wall to the far boundaries (Figure 4). The first cell size is such that the dimensionless normal coordinate y^+ remains less than 0.7 for all the handled flow conditions, and a constant cell size ratio of 1.04 is applied to the first 48 cells generated in the normal direction to the wall.
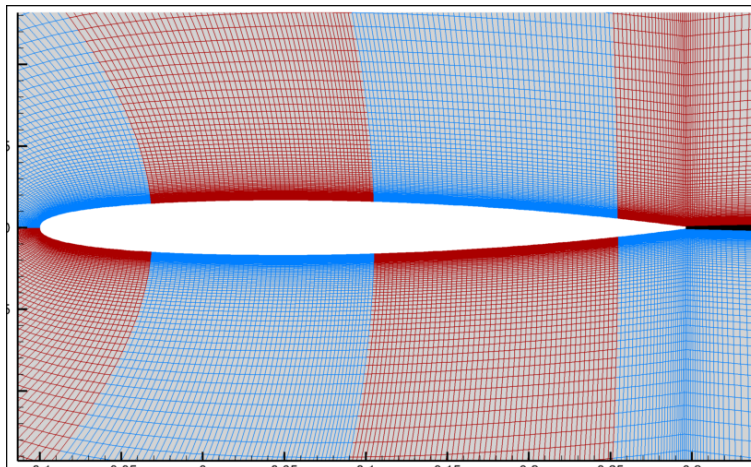

Figure 4: Mesh around the STUNTT airfoil

First simulations were carried out in the case of the triggered transition represented numerically by fully turbulent flows at the transonic Mach number 0.77. A very good agreement was noticed as long as no shock occurs. For transonic flows, discrepancies arose in the region upwind the shock on the upper surface and also in the shock location. An attempt to model the CAD-CUT® strips by a simple triangular shaped bump yielded a pressure distribution in the leading edge area closer to the experiments (Figure 5). Nevertheless the triggering strips modeling was beyond the scope and further simulations were performed using the smooth airfoil mesh.
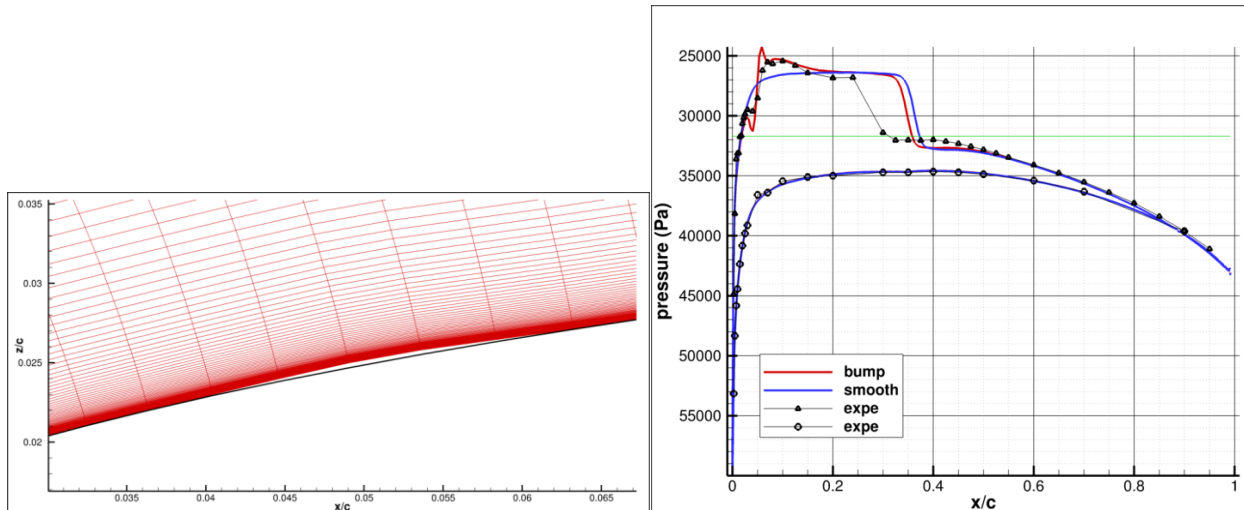
*Figure 5: Airfoil with the bump (left, the black line plots the initial airfoil) and pressure distributions at Mach=0.77 and α=1°
(right)*

4   RESULTS AND ANALYSES

4.1   Static results and analyses

4.1.1   *Aerodynamic polars*

The global aerodynamic lift and moment coefficients for the free and triggered transition are displayed in Figure 6. The lift coefficient shows a pretty linear variation with the pitch angle:

- for low subsonic flows (M=0.5), one may note the straight variation of the lift coefficient with the incidence within the range of pitch angles tested;
- for high subsonic flows (M=0.68), the slope of Cl is also constant up to approximately 2.5°, which corresponds to a shock arising;
- similarly, for transonic flows (M=0.77), the change in the slope occurs for a smaller incidence also related to the compression shock birth (about 1°).

When the flow over the airfoil is fully turbulent, the aerodynamic curves remain pretty similar although the free transition configurations exhibit at the higher angles, a greater Cl or Cm (almost 100 lift counts at M=0.77, 1 lift count = 0.001). This conclusion has to be related with the pressure distribution differences highlighted in the next section.

This behaviour is found by the numerical simulations. As an exemple, Figure 7 plots the lift vs the angle of attack and the transition locations on the upper surface computed using the 4 transition models. The lift slope change due to the shock arising is well captured by all the transition models. The lift evolutions computed with ISES and the transport equation formulation of the AHD model (AHD_EQ, blue curves in Figure 7) are in a very good agreement with the experimental ones. A good agreement was also found out with the Menter-Langtry model (green curves) for angles of attack up to 2° at which the pre-stall lift loss seems to start. The stall angle seems then to be under estimated. When the AHD criteria is used (red curves in Figure 7Figure 7: Lift evolutions (left) and transition locations on the upper surface (right) with respect to the incidence for flows with a free transition at Mach=0.77.**Erreur ! Source du renvoi introuvable.**), a good agreement with

10

the experiments is observed at angles of attack at which no shock occurs. For higher incidences the lift evolution is linear up to 2.5° under estimating the pre-stall stage.
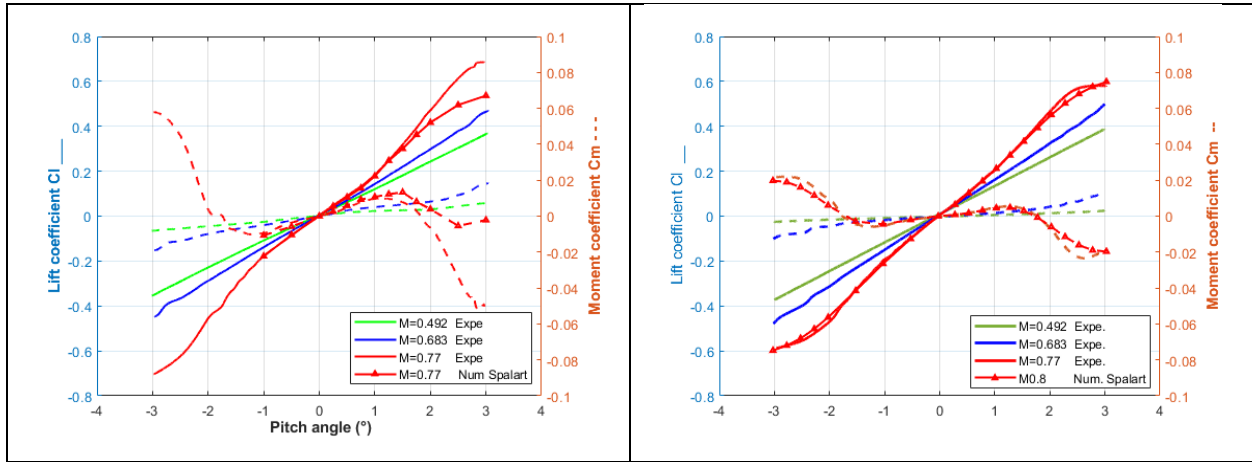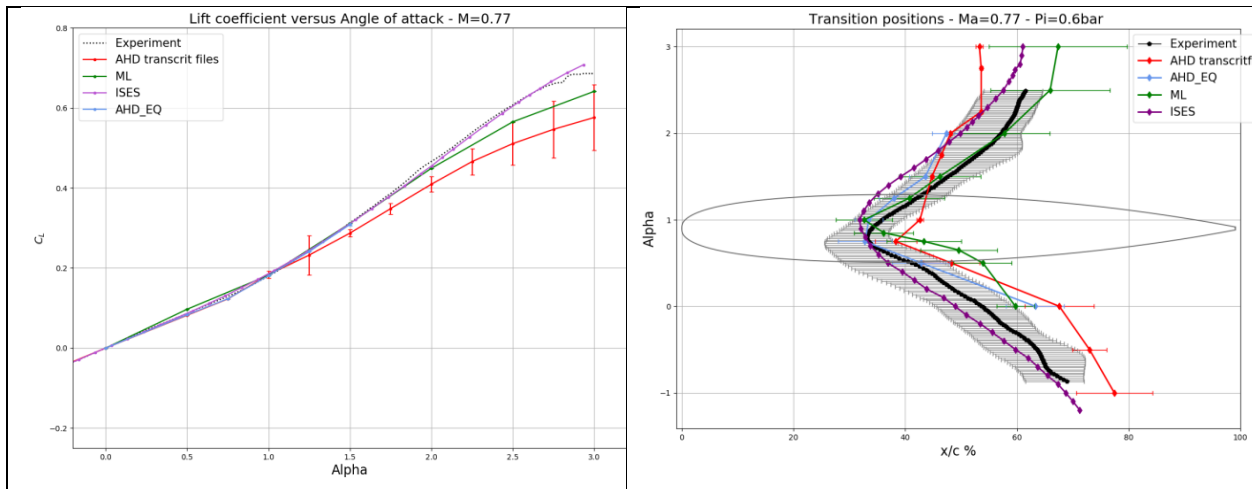

Figure 6: Lift (straight lines) and moment (dotted lines) polar curves: free transition (left figure); triggered transition (right figure). Single lines refer to experimental data, lines with triangle markers refer to numerical simulation using Spalart Allmaras)

Figure 7: Lift evolutions (left) and transition locations on the upper surface (right) with respect to the incidence for flows with a free transition at Mach=0.77.

4.1.2   Pressure distributions and transition analyses

Suction surface pressure distributions versus chord at different pitch angles are gathered in Figure 8 to Figure 9 for both free and triggered transition configurations.

For low subsonic flows (M=0.5), the pressure distributions are smoothly increasing downstream and do not show any shock. Obviously the NLF and triggered configurations are pretty similar. The only difference comes from the presence of the CAD-CUT® strips on the triggered transition configuration for all the pitch angles; it is characterized by an abrupt variation of the pressure in the 5% chord leading-edge region.

For high subsonic flows (M=0.68), the outbreak of a weak shock can be seen on the upper surface, starting from medium angles of attack (2°-2.5°). Once again, both "free transition" and "triggered transition" configurations exhibit almost the same chordwise pressure distributions except in the

leading edge region where pressure bumps linked to the CAD-CUT® strip can be seen for the triggered configuration.

For transonic flows (M=0.8), the shock occurrence starts at a pitch angle about 0.9° and then is moving pretty quickly downstream with increasing angles (shock located approximately at 60% chord for a pitch angle equal to 2.5°). The region of the upper supersonic local flow is increasing with the pitch angle, extending to almost 70% of the chord range for pitch angles equal to 2.5°.

It is observed that laminarity has an impact on several fields of the airfoil aerodynamics. One can see that, whatever the Reynolds number, the shock location for a NLF configuration is more shifted downwards than it is for a triggered configuration; making the pressure integration over the whole chord and consequently the global lift and moment coefficients increasing likewise. Additionally, considering that these changes are more important at higher pitch angles, this explains why the increase of the lift and moment coefficients noticed previously is concerning mostly the higher pitch angles (see 4.1.1).

Besides, if we consider that an estimation of the shock strength is related to the variation of pressure from each side of the pressure increase, we infer from the pressure distributions that the shock strength is slightly greater for free transition flows than for triggered ones. This conclusion is worth whatever the Reynolds number.

It should be noted also that the pattern of the pressure distribution ahead of the shock differ according to the type of configuration:

- When looking at a free transition configuration, the pressure shape presents over almost 10% chord length, a slight increase followed by a small plateau. This behaviour has been found also in the numerical simulations and is related to a separation bubble just ahead of the shock where the wall shear stresses are by the way close to zero.
- When considering a triggered transition, this pattern does not exist anymore and the pressure plateau is filled out, providing an additional, though tiny, local increase of lift.

Finally, as the angle of attack is increasing, the transonic laminar airfoil exhibits some unsteadiness located rather near the shock region but also in the plateau region. This feature is clearly visible in the pressure time evolutions plotted in Figure 13 to Figure 14; when the flow is fully turbulent (tripped configuration), the pressure oscillations upstream of the shock disappears. The single predominant frequency of these pressure fluctuations is approximately 1050Hz (giving a chord related Strouhal of 1.5). Figure 10 displays a power spectral plot of the whole set of the chordwise unsteady pressure signals for an angle of attack equal to 2.5°; it shows that this significant peak occurs between 50% and 80% chord which corresponds to the bulb separation region followed by the shock-downstream zone.
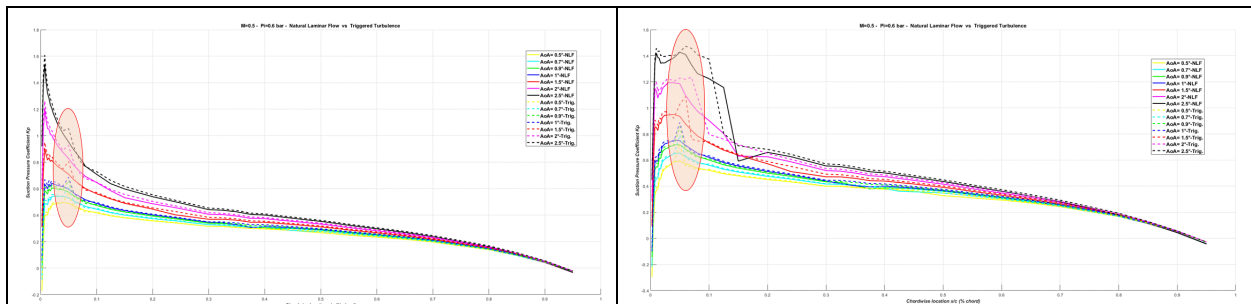
Figure 8: Suction surface pressure coefficient distribution for free (straight lines) and triggered (dotted lines) transition configurations. M=0.5, Pi=0.6b (left figure); M=0.68, Pi=0.6bar (right figure). Pinkish ellipses highlight the CAD-CUT® strips perturbation
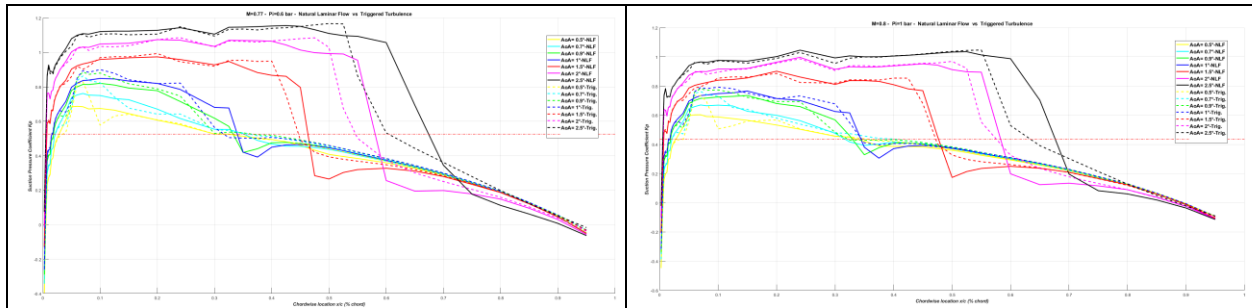

Figure 9: Suction surface pressure coefficient distribution for free (straight lines) and triggered (dotted lines) transition configurations. Dash-dot lines correspond to the critical pressure coefficient. M=0.77, Pi=0.6b (left figure); M=0.8, Pi=1bar (right figure)
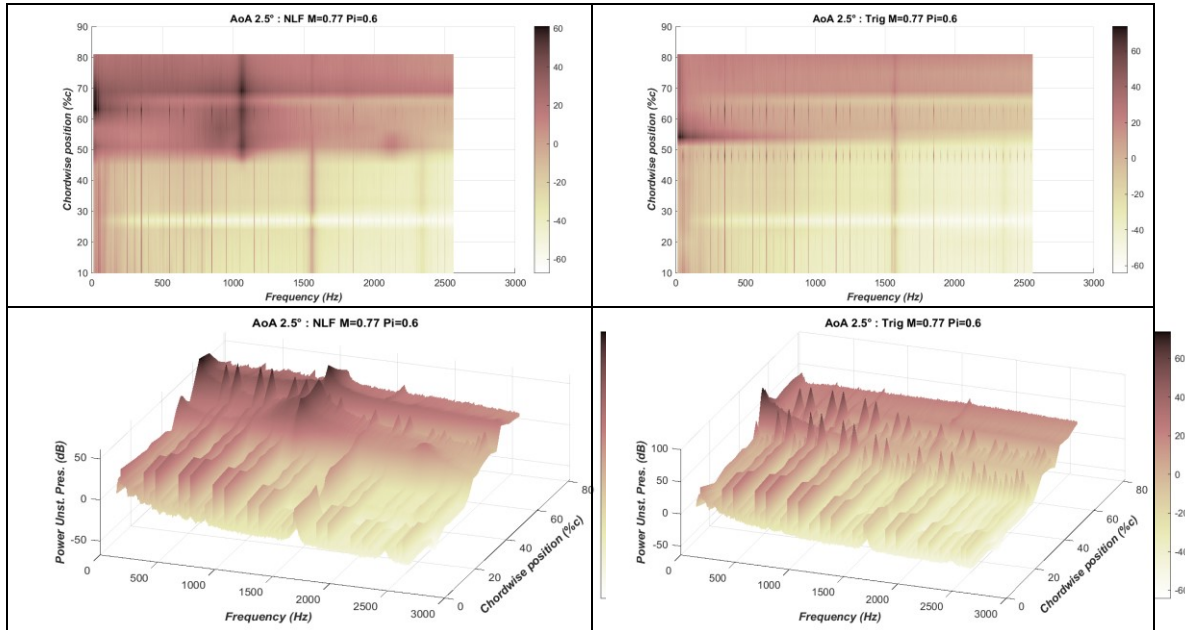
Figure 10: Power spectral density of upper section pressure: natural laminar flow (left); full turbulent flow (right). Upper plots show 2D upper view.

The laminar to turbulent transition was defined thanks to the analysis of the wall shear stress time signals given by hot films. These latter have thus been calibrated in laboratory according to the general King's law relating the output voltage signal E and the wall shear stress τ_p :

$$E^2 = A + B \cdot \tau_p^n$$

where A, B and n are coefficients coming from the calibration, the initial wind tunnel test conditions and the considered test point parameters (local Mach, local pressure, air density, dynamic viscosity,…).

In order to extract the transition chord location, the following post-processing process was applied to each hot film at each time step:

- Setting an appropriate sliding time window whose length is fitted to the pitch angle rate of the test point
- Processing the RMS of the time wall shear stresses within this window
- Searching the chord position corresponding to a sizeable change of the RMS signals of the whole set of hot films, from a low level to a high level. The method used here is mainly based on the analysis of the gradient with respect to the chord location [8].

It should be noted that the onset of laminar to turbulent transition is often linked with time fluctuations implying larger standard variations values. Therefore, another way of determining the transition location could be by looking for the maximum standard deviation variation over the set of hot films.

As a result of the post-processing of the quasi-steady polar points, Figure 11 displays pseudocolor surface plots of the wall shear stress τ_p for the 3 Mach numbers, the color scale giving the magnitude of τ_p for each couple of point [chordwise position, pitch angle]. In this figure, the upper views relate to the free transition configuration while the lower ones correspond to the triggered transition point. The color scale has been chosen so that cold colors (deep blue) are linked to low shear stresses (or mostly laminar flow) while hot colors (orange – yellow) indicate a high value (or mostly turbulent flow). The reader will at first sight be able to detect the different local flow changes like the boundary layer transition or the shock with boundary layer separation.

For subsonic inflows (M=0.5), when increasing the angle of attack, the transition line remains first fixed rearward at about 65% chord (-3°< AoA <-1.5°), then moves towards the leading edge and lastly stays at around 10% chord. It should be noted that apparently, the hot films located between 42% chord and 60% chord were polluted, the effect of this being a turbulent zone visible in the upper left plot. Appropriate corrections were applied for the setting of the transition onset in this region (see Figure 12).

For transonic inflows (M=0.77), the transition line exhibits a V-shaped variation:

- The 1st part, corresponding to an increase of the pitch angle from -3° to about 0.5° is similar to the one observed at M=0.5, i.e. the transition position remains at first confined rearwards for angles up to 1° (~60%-70% chord) then moves frontwards pretty quickly reaching 35% chord for a pitch angle equal to about 0.5°.

- The 2nd part corresponds more or less to the moving position of the upper surface compression shock with increasing angles from 0° to 3°. The wall shear stress just ahead of the shock is null which should correspond to a flow separation bubble just upstream of the shock and the transition is located at the shock position, moving downstream with him. The length of this separation region slightly increases with the pitch angle from nearly 4% chord to 10% chord. It should be noted that the region located between 5% chord and 20% chord exhibit a higher turbulence rate which could be linked to a minor leading edge contamination.

The experimental evolution of the transition location on the upper surface is globally well reproduced by the simulations using the 4 transition models (see Figure 7: Lift evolutions (left) and transition locations on the upper surface (right) with respect to the incidence for flows with a free transition at Mach=0.77. right): the transition runs from about 50% of chord to about 35% for angles of attack inducing no shock (from 0° to 0.75° or 1°), then moves downstream up to 60% of

chord when a shock occurs (incidences from 0.75° to 3°). Nevertheless, the transition is always attached to the shock when predicted using the Menter Langtry model whereas it is always detached and upstream of the shock when computed using ISES. Both AHD models (criteria and transport equation formulation) provide a transition attached to the shock for incidences up to 1.5° and a detached and upstream for higher incidences.

For the transonic triggered case (lower right plot), the wall shear stress is logically high. However, for angles greater than 2°, the region located near the trailing edge exhibits a reduced, indeed very small wall shear stress. The boundary of this "relaminarized" zone is related to the shock position at these angles.
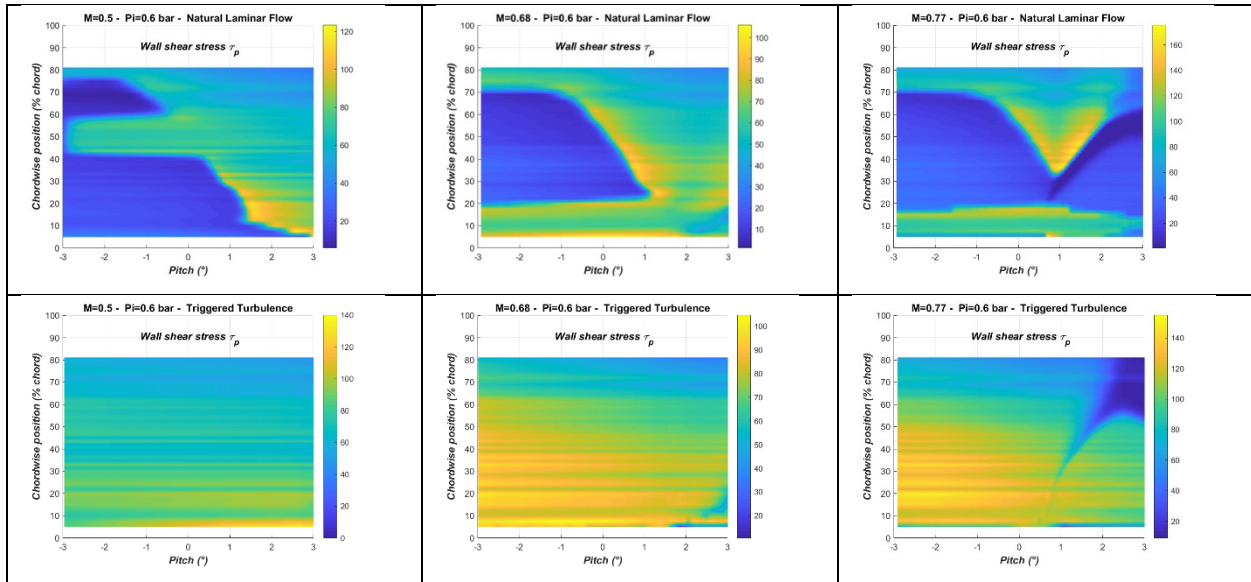
Figure 11: Wall shear stress variation with quasi-steady pitch: M=0.5 (left figures); M=0.68 (middle figures); M=0.77 (right figures). Upper plots: natural laminar flow; lower plots: triggered turbulence.
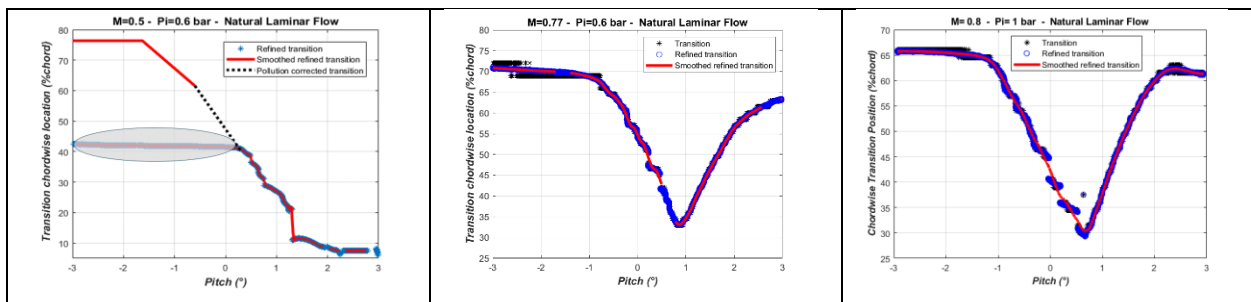
Figure 12: Laminar to turbulent transition variation with quasi-steady pitch angle. M=0.5 Pi=0.6bar (left; the grey ellipse points out the erroneous line transition due to polluted hot films in the [42% 60%] chord range and corrected by the black dotted line); M=0.77 Pi=0.6bar (middle); M=0.8, Pi=1bar (right).

A comprehensive analysis of both pressure and shear stress distributions on the upper surface for either a natural transonic laminar configuration (Figure 13) or a tripped one (Figure 14) allows to better understand and strengthen the above results. In these figures, several specific angles of attack

are displayed, corresponding to a zero lift incidence with no shock, an incidence corresponding to the shock arrival (AoA~1°) and some values with the shock moving rearwards (1°<AoA<3°):

- When the shock is present, the transition location stays attached to this latter and features a laminar separation bubble whose length is progressively increasing with the pitch angle, ranging from 4% chord (at 1°) to approximately 10% chord at 3°.
- The unsteadiness of the τ_p time signals in the turbulent zones are clearly seen.
- The start of relaminarization rearward the shock in the full turbulent configuration coincides with the shock.
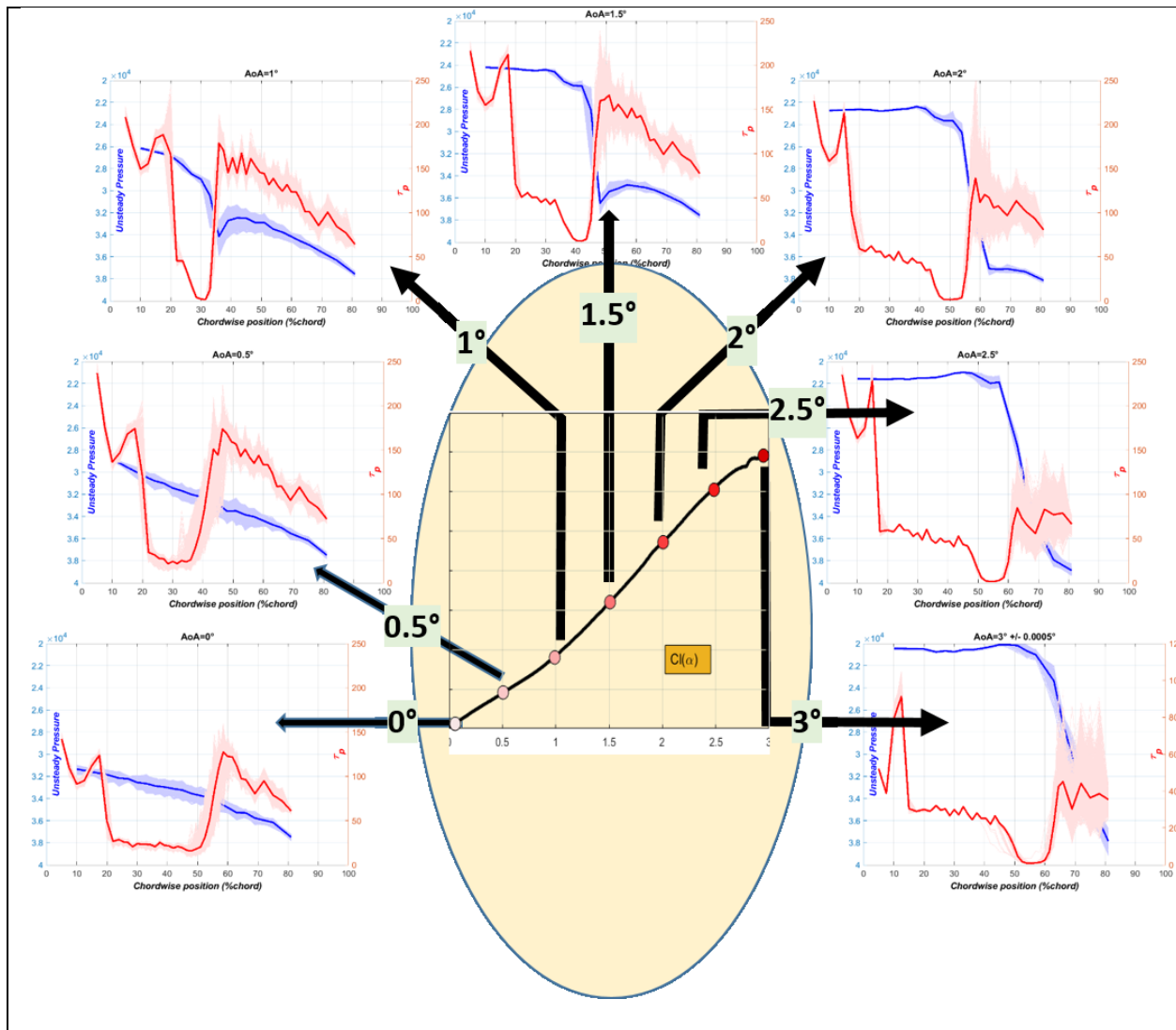
Figure 13: Upper section unsteady pressure (blue) and wall shear stress coefficient (red) distributions for selected pitch angles. Transonic natural laminar flow configuration. Deep color curves correspond to the mean time values.
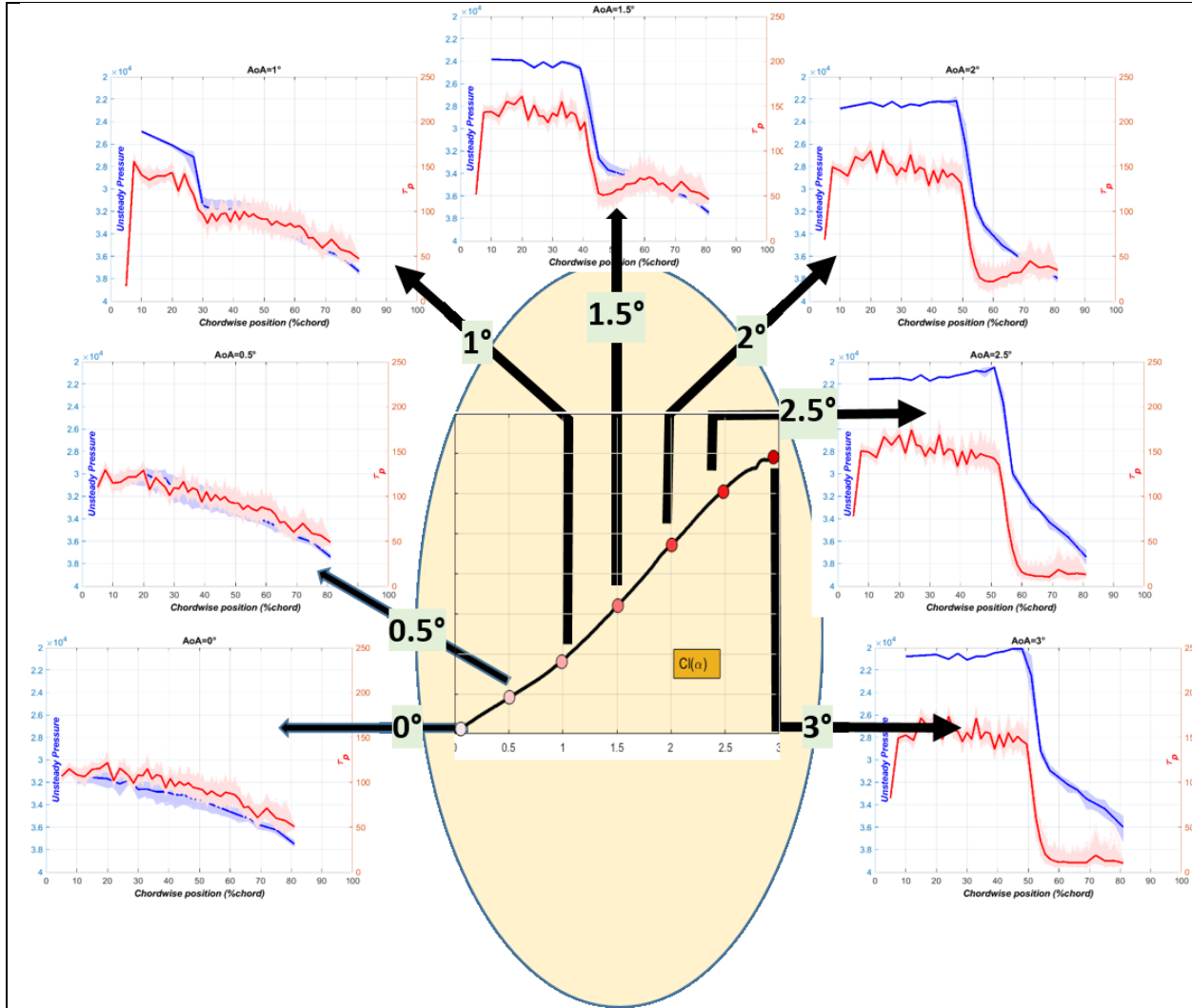
Figure 14: Upper section unsteady pressure (blue) and wall shear stress coefficient (red) distributions for selected pitch angles. Transonic triggered flow configuration

4.2 Unsteady results and analyses

4.2.1 Unsteady loads

The plots of the unsteady lift and moment coefficients derived from unsteady pressure measurements, as a function of the angle of attack or as a function of time for sinusoidal pitching motions of the model, are shown in the following sections. They will illustrate the influence of key parameters such as the Mach number, the reduced oscillation frequency ω_R, the laminarity or the Reynolds number. The moment coefficients reference point is the leading edge. Generally speaking, the plots show the classical hysteresis loops similar to those obtained using basic Theodorsen theory.

The reader is warned that due to the lack of fully functional unsteady pressure sensors near the leading edge and the trailing edge of the profile, the unsteady lift plotted in the following figures corresponds to the integration of the interpolated pressure only between 10% chord and 80% chord which could explain the slight offset noted between mean unsteady values and the steady values

(these latter beeing derived from the static pressure taps integration ranging from 0 to almost 100% chord). Therefore, in order to ease the comparisons for some configurations, the steady and unsteady chordwise integrations have been made compliant by performing an integration of the steady pressure over the same chordwise range e.g. [10% 80%] chord.

The influence of Mach number is reported for different mean angles (0°, 1°) and the same oscillation frequency (ω_r= 0.1) and dynamic pitch range (0.5°). For low and high subsonic flows, the phase delay between the unsteady lift coefficient and the pitch oscillation is almost negligible. When the flow becomes transonic, it becomes more apparent as shown by the left plots in Figure 15 and Figure 16.
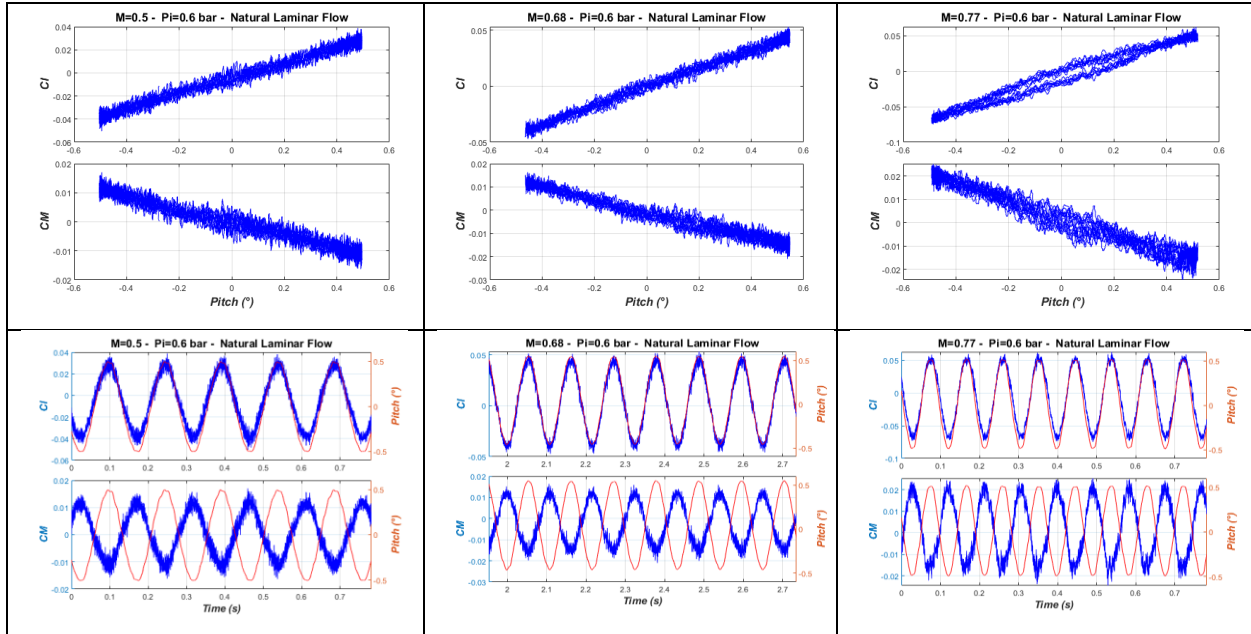
Figure 15: Unsteady lift and moment coefficients at different Mach numbers (reduced oscillation frequency ~0.1 ; pitch = 0°±0.5°). Red curves correspond to the time pitch oscillation, blue curves correspond to the Cl or Cm time variations).
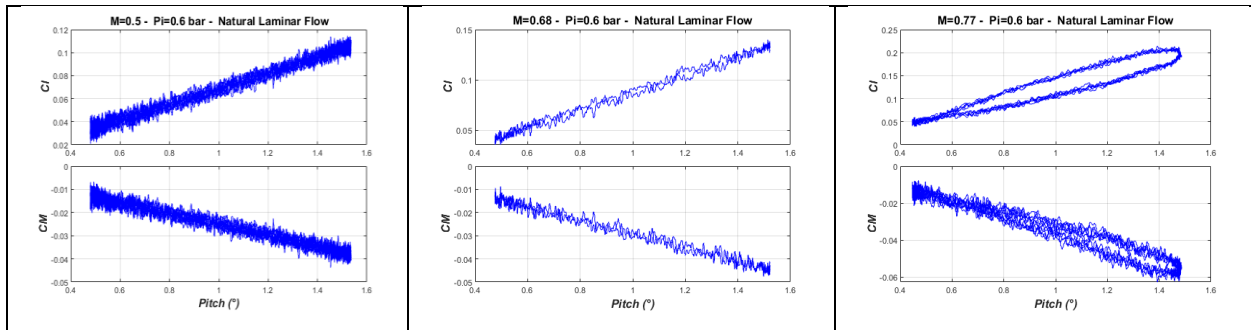
Figure 16: Unsteady lift and moment coefficients at different Mach numbers (reduced oscillation frequency ~0.1; pitch = 1°±0.5°)

The effect of the laminarity on the unsteady loads is displayed in Figure 17 which shows, for each of 2 reduced frequencies (ω_R=0.1 and ω_R=0.3) the experimental lift and moment coefficients for a free transition configuration and the corresponding triggered transition one. The influence remains tiny at transonic fields, translated into a minor shift of the whole aerodynamic coefficients loops. Besides, it is shown that the central points of these unsteady lift loops are indeed coinciding

with the corresponding steady lift value (dotted lines) when both are the result of an integration over the [10% 80%] chordwise range.

It should be noted that the effect of laminarity was found negligible at low Mach numbers (M=0.5) and imperceptible at higher Mach numbers (M=0.68).
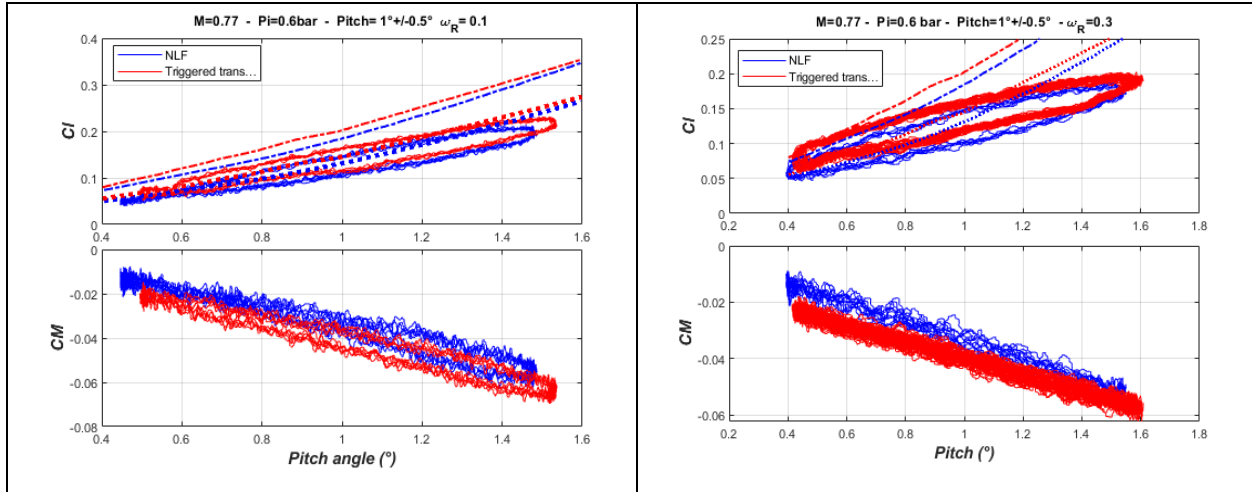

Figure 17: Impact of laminarity on unsteady lift and moment coefficients in transonic flow. Dash-dotted line correspond to steady lift integrated over [0% 100%] chord; dotted lines correspond to steady lift integrated over [10% 80%] chord. (Left plots : reduced oscillation frequency ~0.1 ; right plots : reduced oscillation frequency ~0.3) . Pitch = 1°±0.5°

The influence of the pitch oscillation frequency is displayed in Figure 18.

The phase of the lift relative to the angular motion is increasing with the oscillation frequency, this change being more pronounced in transonic regimes than the one observed in a subsonic flow.

Moreover, the slope of the unsteady lift coefficient is decreasing with the oscillation frequency either during the upstroke or the downstroke. As a result, the lift range variation ΔCl during the oscillation period weakens with ω_r (from about 0.15 at ω_r=0.1 to 0.08 at ω_r=0.5). The mean slope of the downstroke lift is more linear than the upstroke one, at least for low oscillation frequencies.
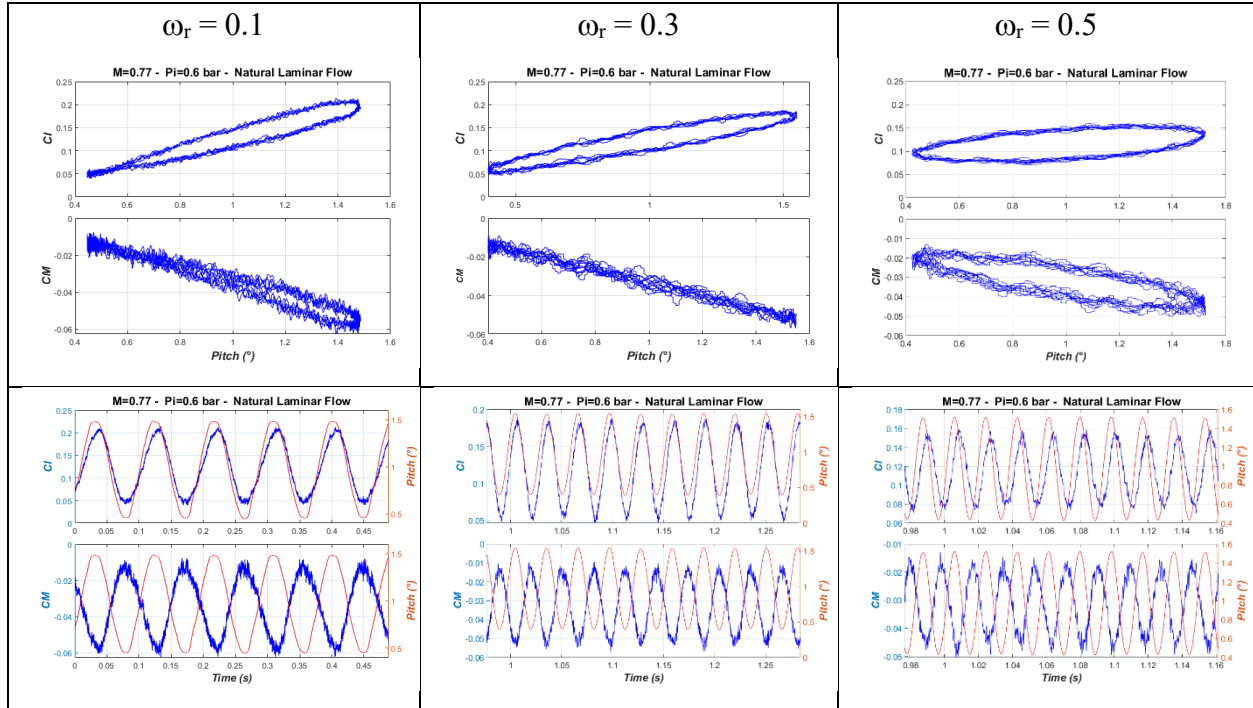
Figure 18: Unsteady lift and moment coefficients for different reduced frequencies (M=0.77 ; pitch = 1°±0.5°)

Numerical investigations have been performed at M=0.77 in order to investigate the aerodynamic response to a forced harmonic pitching motion (mean incidence=1°, dynamic amplitude = 0.5°, reduced frequency ω_r=0.1).

The simulations were carried out using the Dual Time Stepping (DTS) time resolution algorithm with at least 128 time steps per period and the AHD criteria for free transition. As recalled above, the experimental unsteady forces are derived from the integration of the pressure measured by functional Kulite sensors ranging from 10% to 80% of the airfoil chord, whereas the experimental static forces derive from static pressure sensors located on the whole chord. The numerical forces are also obtained from the pressure integration on the whole chord. Since the forces due to the pressure distribution on the first 10% of chord are significant, and in order to be able to compare all the aerodynamic forces, the experimental dynamic forces are plotted on the figures with a constant correction (about 65 lift count for triggered and 56 for free transition) such that the middle of the hysteresis loop at an incidence of 1° matches the experimental static force at the same incidence. This assumption is validated by the fact that :

- on one hand, the difference between the 1° experimental steady lift integrated over [10% 80%] and over the whole chord is about 60 lift count;
- on the other hand, both experimental static and central hysteresis loop values for 1° (derived from a pressure integration over [10% 80%] chord turned out to agree), see Figure 17.

 Figure 19 plots the lift and the transition location evolutions from both the experiments and the numerical simulation. A good agreement can be noticed. The shape of the hysteresis loop of the lift, its orientation and width, are close to the experimental ones, showing that the amplitude of the aerodynamic force induced by the pitching motion and its phase shift with the incidence evolution

are well predicted. The double loop of the hysteresis cycle of the transition location on the upper surface of the airfoil is also well captured by the numerical simulation.
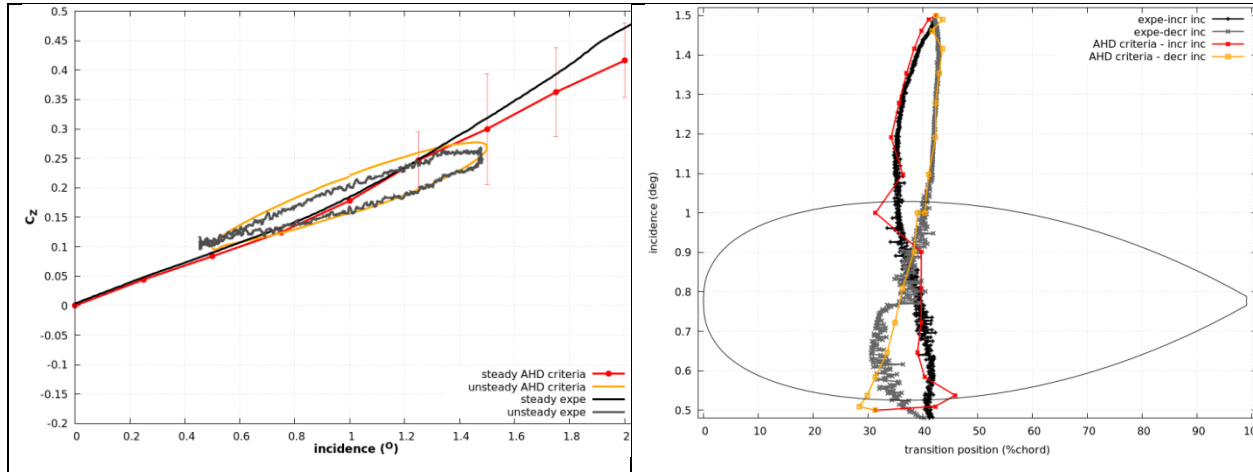

Figure 19: Lift (left plot) and transition locations (right plot) evolutions with incidence.

Figure 20 shows the lift evolutions for the free and triggered transitions. Both numerical and experimental curves exhibit a linear static behavior with a slope change when a shock arises. This slope change is higher when the transition is free, what is also captured by the numerical simulations. The experiments have shown similar dynamic hysteresis loop (orientation and loop width) when the transition is free or triggered. The numerical simulations have also exhibited this similarity. One can nevertheless observe discrepancies between the experimental and numerical dynamic lift evolutions for the smaller incidences. In terms of pressure distribution, the numerical simulations modeling the transition or assuming the flow fully turbulent provide similar distributions during the pitching cycle, with small discrepancies in the shock strength, as can be seen in Figure 21 representing the pressure distributions and contours at 4 instants of the cycle. Looking at only the free transition case, one can notice from the experiments that the shock oscillates for the cycle and disappears for low angles of attack in the last quarter of the period (ascending stage). The shock motion is also predicted by the numerical simulations, but unlike the experiments the shock never disappears. The numerical simulation tends then to underestimate the amplitude of the variations of both the shock strength and location.
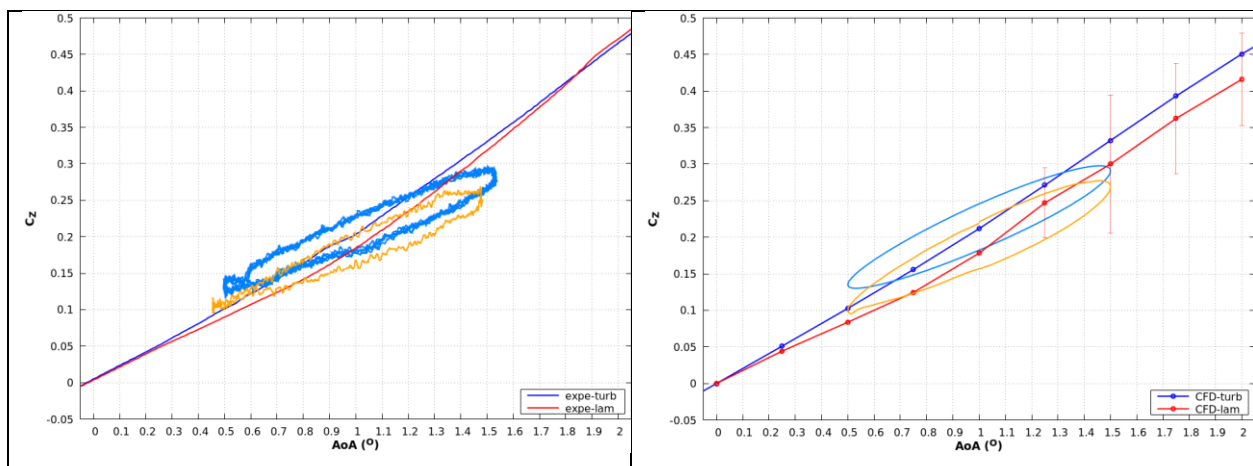

Figure 20: Lift evolutions for triggered and free transition obtained experimentally (left) and numerically (right)
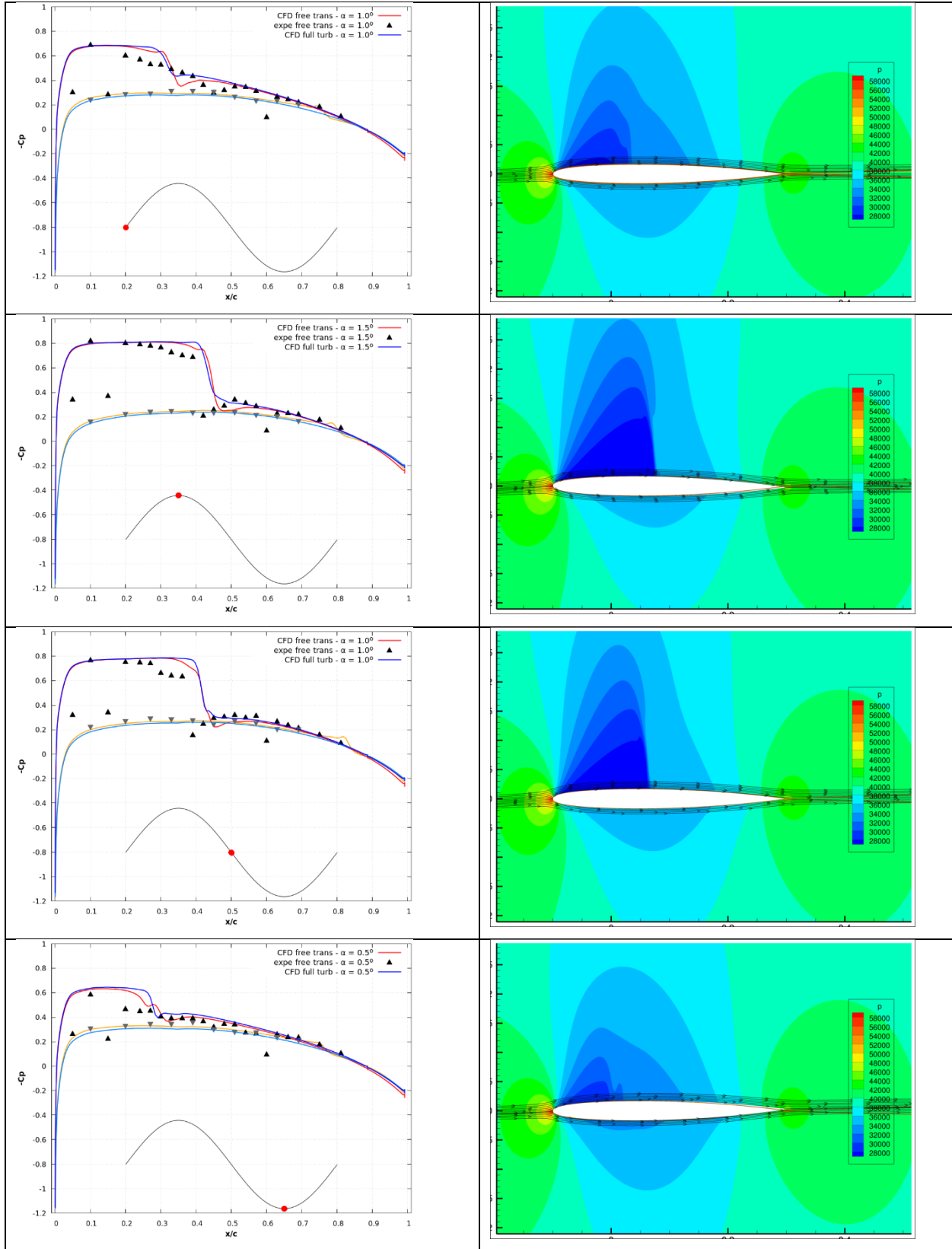
Figure 21: Pressure distributions at 4 instants of the pitching oscillation cycle of the airfoil. The pressure contours come from numerical simulations using the AHD criteria.

The impact of the Reynolds number on unsteady loads was analyzed in transonic cases for several mean pitch angles and/or different ω_r (see Figure 22).

Besides the fact that the phase lag of unsteady loads versus the pitch angle is more visible at higher ω_r, one may notice also a small increase of the phase lag magnitude at small ω_r and rather a slight decrease at higher ω_r.
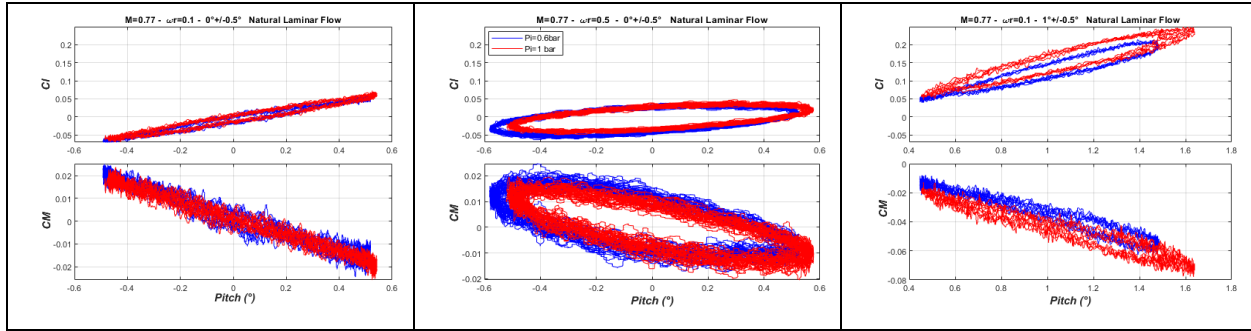
Figure 22: Unsteady lift and moment coefficients for 2 Reynolds numbers
(reduced oscillation frequency ~0.1 and 0.5 ; pitch = 0°+0.5° and 1°±0.5°).

In order to investigate the impact of the oscillating transition on the unsteady loads of a free laminar transonic case, aerodynamic derivatives have been carried out for the different tested oscillation frequencies and for 3 steady angles of attack (0°, 0.5° and 1°). The amplitude of the dynamic pitch was kept constant and equal to 0.5°. Figure 23 displays the magnitude and phase variation of the complex lift derivatives wrt the reduced frequency ω_r.

The magnitude of the derivative is decreasing with the oscillation frequency; no specific aerodynamic resonance can be observed for the tested frequencies analyzed. The discrepancy seen between the 3 oscillation pitches cases concerns only the lowest frequencies, but cancels for the highest ones. This remark concerns the magnitude as well as the phase components of the lift derivatives.
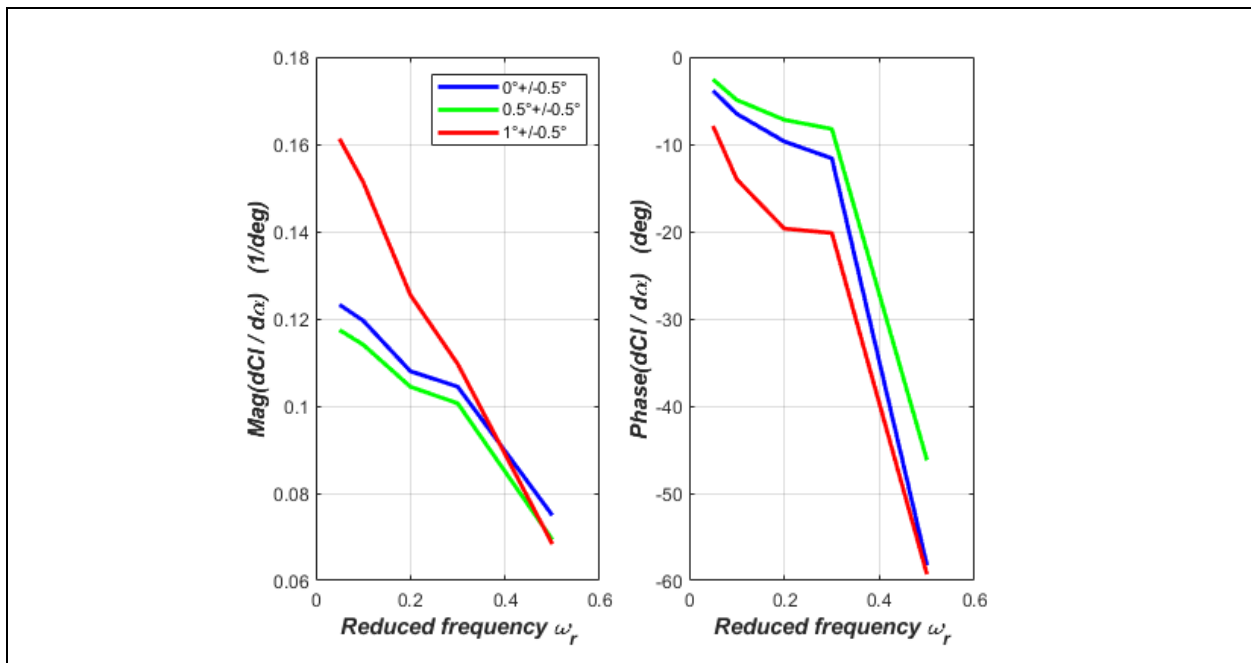

Figure 23: Lift coefficient derivative (M=0.77, different pitch oscillations)

A more thorough analysis has also been carried out by considering the distribution of the unsteady local loads wrt the dynamic motion. The resulting coefficients are the values (computed at the frequency of oscillation) of the complex transfer function between normalized time unsteady loads and the corresponding time pitch motion. The processing was done for the 3 above-mentioned oscillations cases and for free and triggered transition configurations (see Figure 24).

Generally, one will observe a reduction of the local unsteady loads coefficients when increasing ωr. More specifically:

- for a pitch angle oscillation equal to 0.5°+/-0.5°, no shock occurs on the suction surface; the unsteady loads differ only in the upstream quarter chord region with a reduction when ω_r is increasing. The sign of the phases on each side of the axis of rotation does not change whatever the frequency.
- for a pitch angle oscillation equal to 1°+/-0.5°, the unsteady local loads present a more important bump centered around 35% chord and corresponding to the shock mean location, whereas the sign of the phases is inverted rearwards a chordwise location about 40% chord.
- for a pitch angle oscillation equal to 1.5°+/-0.5°, the same conclusions can be drawn except that the phase chordwise sign changing occurs, in agreement with the shock displacement, a little bit rearwards (about 50% chord). Moreover, the highest coefficient values remain located near the pitch axis of rotation, hence reducing their participation in the resulting unsteady moment coefficients.

Lastly the unsteady loads coefficients distributions are more or less similar for a free transition configuration or a triggered one; one major difference concerns the axis of the bump which is located a little bit upstream for the triggered transition case since it is linked to the location of the shock which follows the same trend (as noted in section 4.1.2). Consequently, the aeroelastic behaviour should not extremely differ.
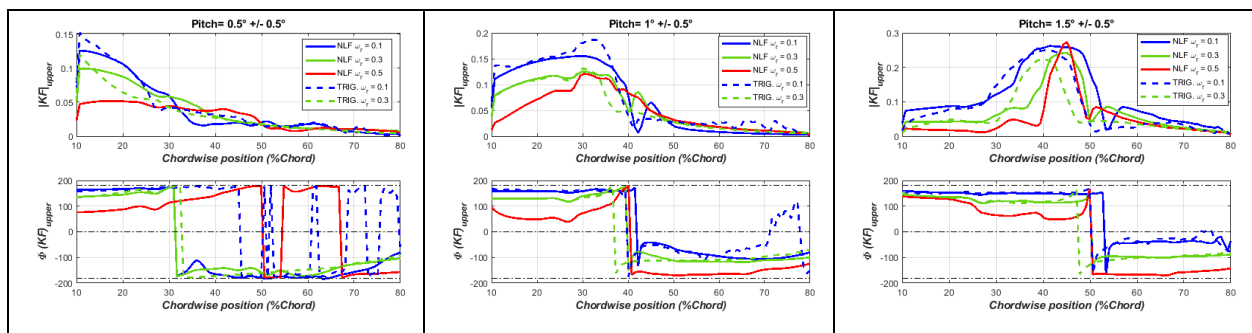

Figure 24: Chordwise distribution of the normalized transfer functions "loads/motion" at the oscillation frequency. Transonic flow.

4.2.2 Unsteady transition analysis

In order to extract the laminar to turbulent transition location from the hot films signals during the dynamic pitch oscillations, several phases have been carried out:

- The 1st step of the processing is the same as the one described in the steady polar points analysis (see 4.1.2**Erreur ! Source du renvoi introuvable.**).
- In a 2nd step, the results are "synchronized" and ordered using a clustering method based on the averaged phase of the pitch signal. This processing allows thus to get the movement

of the transition location during the different phases of the oscillation: the figures shown below include the variation of the transition location with respect of the upstroke part of the oscillation (red color plots) or the downstroke part of the oscillation (blue color plots).

Moreover, the steady variation of the transition location (green color) is overlaid on some plots in order to understand the dynamic behaviour of the transition.

The effect of the Reynolds number on the transition onset in transonic regimes is displayed in Figure 25 to Figure 27 and corresponds to 3 mean pitch angles (0°, 0.5° and 1°) and low to high ωr. From these figures, one may notice that the transition variation range is getting narrower with an increase of the oscillation frequency; this conclusion being not modified by the change in Reynolds number. Furthermore, without a shock present on the suction surface (corresponding to a mean angle of 0° for instance), the chordwise span of the transition motion is also decreasing when the Reynolds number rises up whereas when the transition is attached to the shock, the chordwise span of the transition motion almost doesn't change.

The phase shift between the upstroke and downstroke transition lines generate for some mean pitch angles multiple loops. This is mainly the case for mean pitch angles above 0.5°(see Figure 26 and Figure 27) where the transition onset is moving consecutively in opposite directions in the same pitching stroke (increasing or decreasing). This direction change of the transition chordwise position (from upstream to downstream or vice versa) is in agreement with the steady variation, as shown in Figure 12.

For a moderate mean pitch angle (0.5°± 0.5°), this occurrence is more pronounced at higher Reynolds while it is the opposite for a higher pitch angle variation (1°± 0.5°).
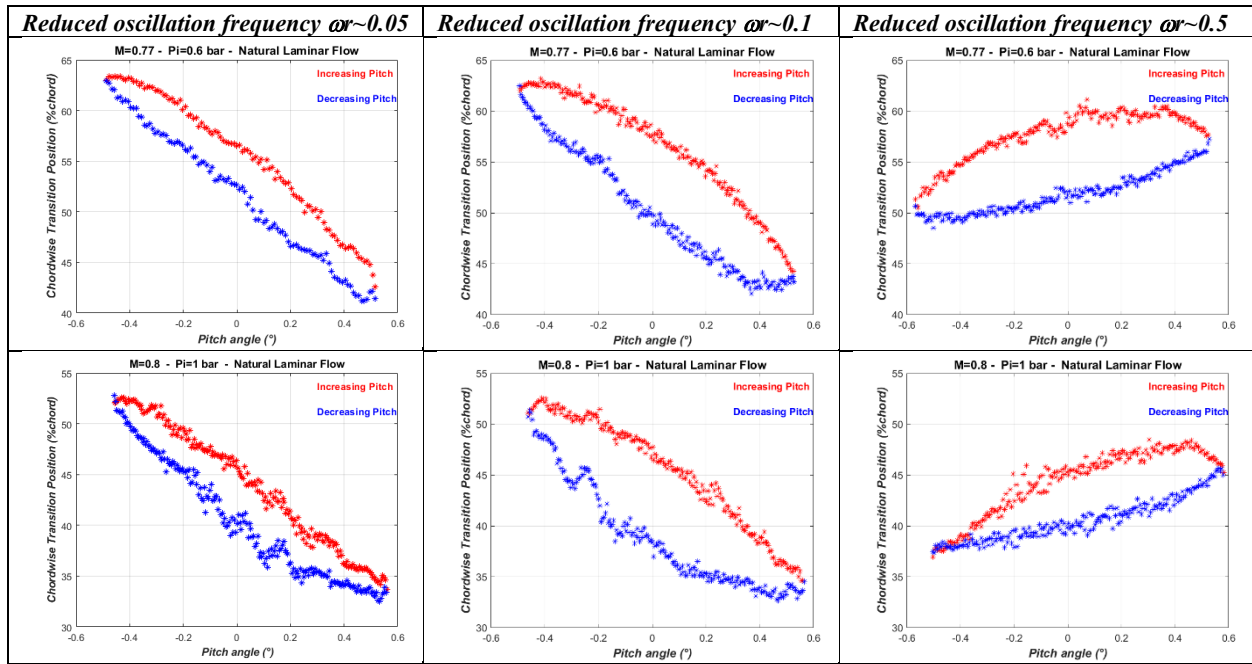

Figure 25: Effect of Reynolds on the transition behaviour at several reduced frequencies : M=0.77 ;pitch =0°±0.5°.
Upper figures : Pi=0.6bar ; lower figures : Pi=1 bar

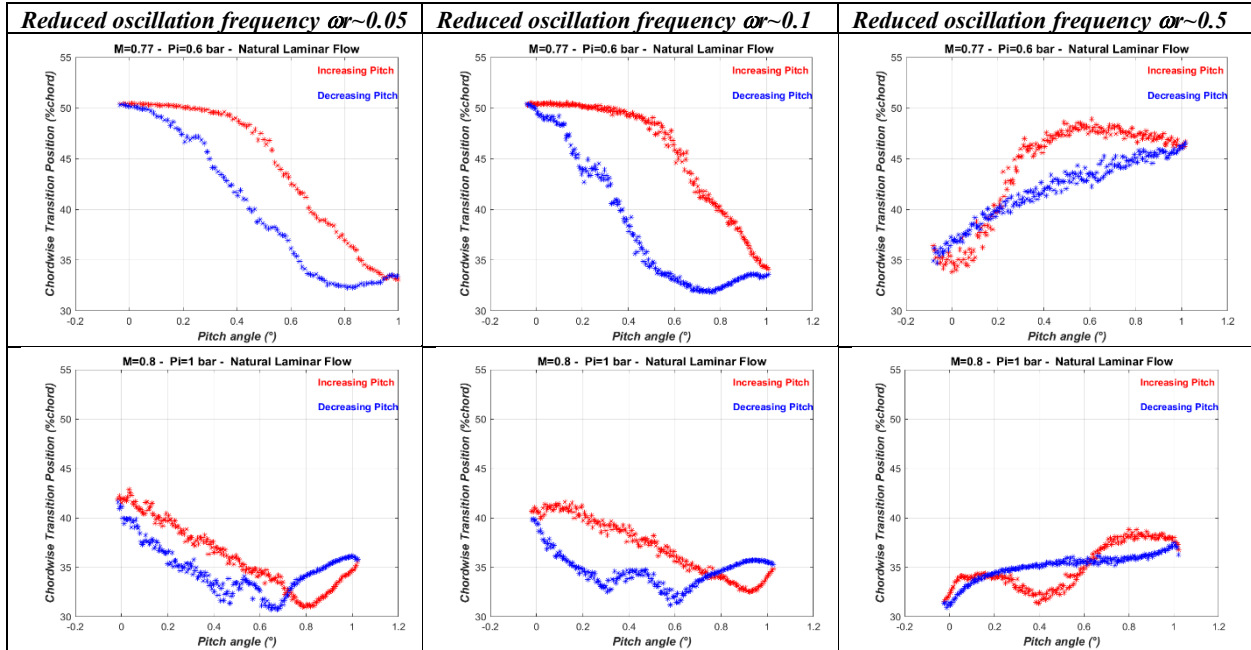*Figure 26: Effect of Reynolds on the transition behaviour at several reduced frequencies : M=0.77 ;pitch =0.5°±0.5°.*
Upper figures : Pi=0.6bar ; lower figures : Pi=1 bar

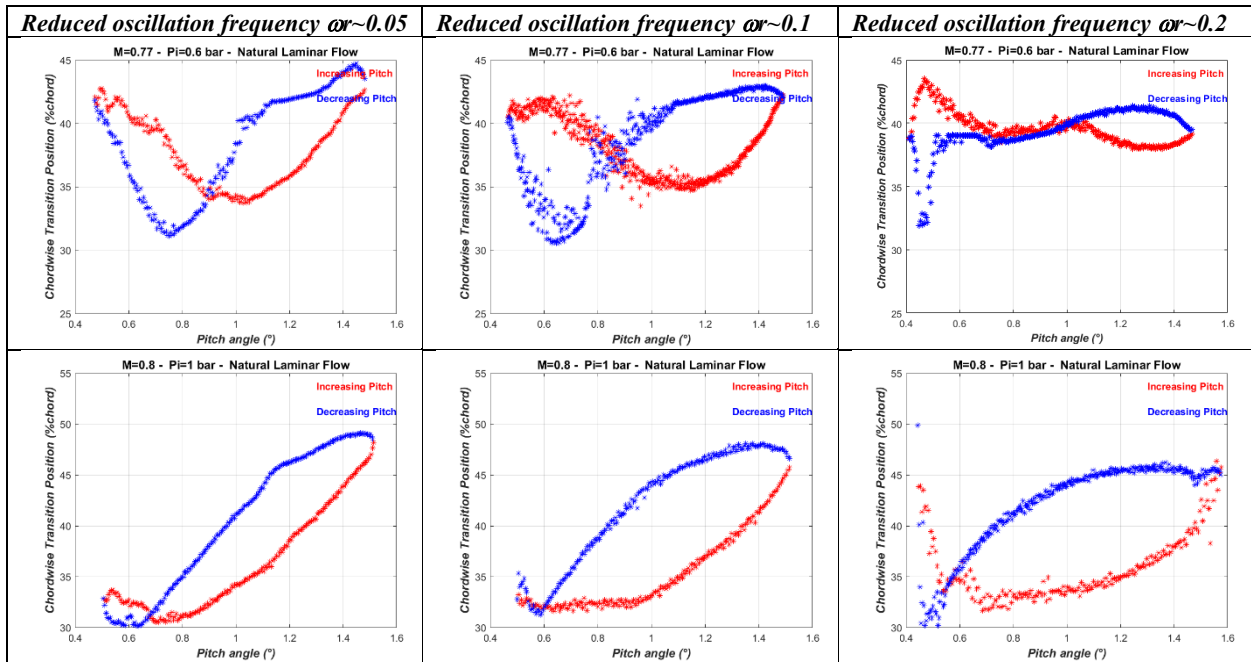*Figure 27: Effect of Reynolds on the transition behaviour at several reduced frequencies : M=0.77 ;pitch =1°±0.5°.*
Upper figures : Pi=0.6bar ; lower figures : Pi=1 bar

The influence of pitch oscillation frequency is displayed in Figure 28 to Figure 30.

For transonic regimes, some general conclusions can be drawn depending upon the mean pitch angle.

For a null mean angle, the lag between the increasing and the decreasing pitch transition lines enlarge with ωr. Thus, the difference of the dynamic transition locations at 0° with respect to the quasi-steady value vary about ± 2% chord at ωr=0.05 and ± 4% at ωr=0.1. Besides, the extent of the overall transition variation during an oscillation is shortened. It is recalled that for the subsonic inflow, increasing ωr will likewise slightly change the phase shift between upstroke and downstroke as well as the transition onset overall range.

Simultaneously, when increasing ωr, the movement of the transition onset with the pitch angle is at first consistent with the quasi-steady movement (i.e. going upstream with increasing pitch and vice versa), but is then inversed at the highest ωr (i.e. going downstream with increasing pitch and vice versa). It is recalled that this case corresponds to a configuration where there is no compression shock on the upper side of the model and where the variation of the transition onset with pitch angle was found pretty linear (see Figure 12).

For a medium mean angle, the difference of the dynamic transition locations at 0.5° with respect to the quasi-steady value vary about ± 5% chord at ωr=0.05 and ± 7.5% at ωr=0.1. The inversion of the chordwise movement of the transition onset is also observed at high ωr.

For the greatest mean angle (~1°) and for all the ωr tested, the upstroke transition chordwise position matches more or less the quasi-steady parabolic variation line with some additional phase shift, the latter growing with ωr, (see Figure 30).

The downstroke chordwise position follows also the same quasi-steady trend except for ωr= 0.5 where the transition position remains almost stuck around 40% chord. Correlatively, the unsteady pressure distribution differs between the upstroke and the downstroke. Figure 31 displays for this purpose, the upper section pressure distribution for some selected angles in the range [1° 1.5°]. It highlights a different pattern for increasing or decreasing pitch angles.

Thus, the downstroke main pressure rise remains more often located around 40% chordwise while softer upstroke pressure rises are fluctuating between 25% to sometimes 50% chordwise.
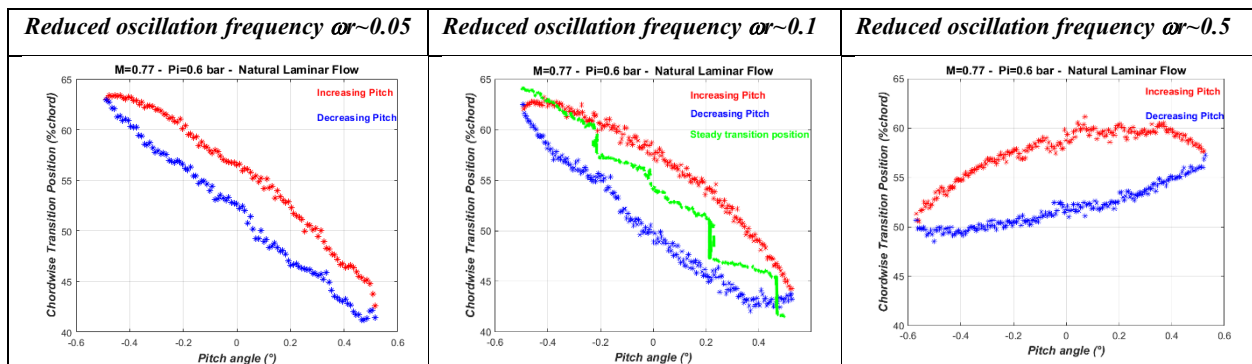

Figure 28: Effect of the pitch oscillation frequency on the transition behaviour : M=0.77 ;pitch =0°±0.5°.
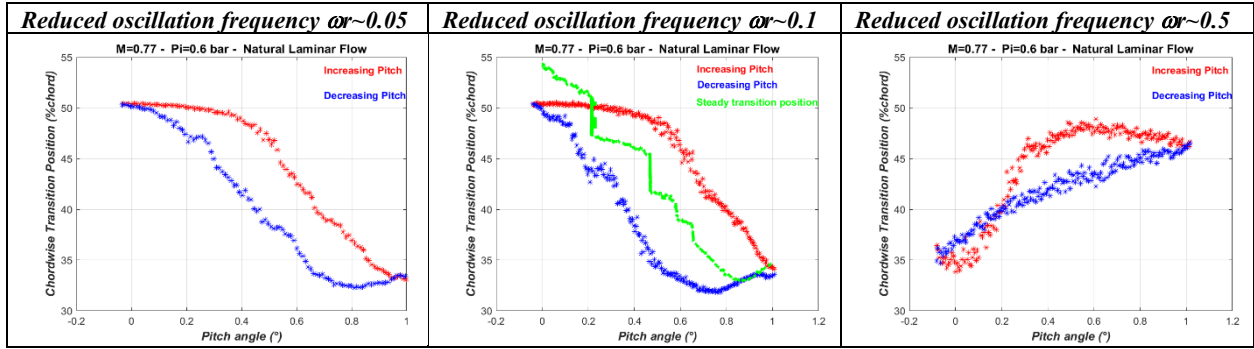*The green line represents the steady transition variation from quasi-steady polars*

Reduced oscillation frequency ωr~0.05	Reduced oscillation frequency ωr~0.1	Reduced oscillation frequency ωr~0.5

Figure 29: Effect of the pitch oscillation frequency on the transition behaviour : M=0.77 ;pitch =0.5°±0.5°.
The green line represents the steady transition variation from quasi-steady polars.

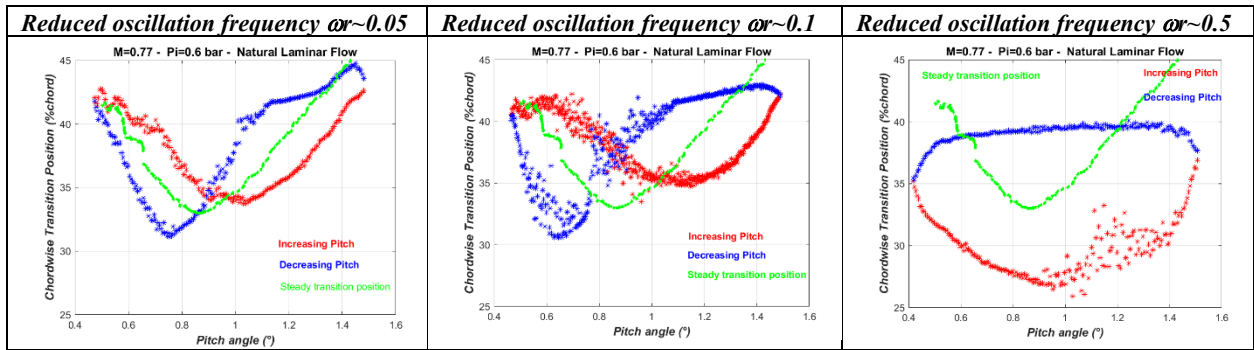| Reduced oscillation frequency ωr~0.05	Reduced oscillation frequency ωr~0.1	Reduced oscillation frequency ωr~0.5

Figure 30: Effect of the pitch oscillation frequency on the transition behaviour : M=0.77 ;pitch =1°±0.5°.
The green line represents the steady transition variation from quasi-steady polars.
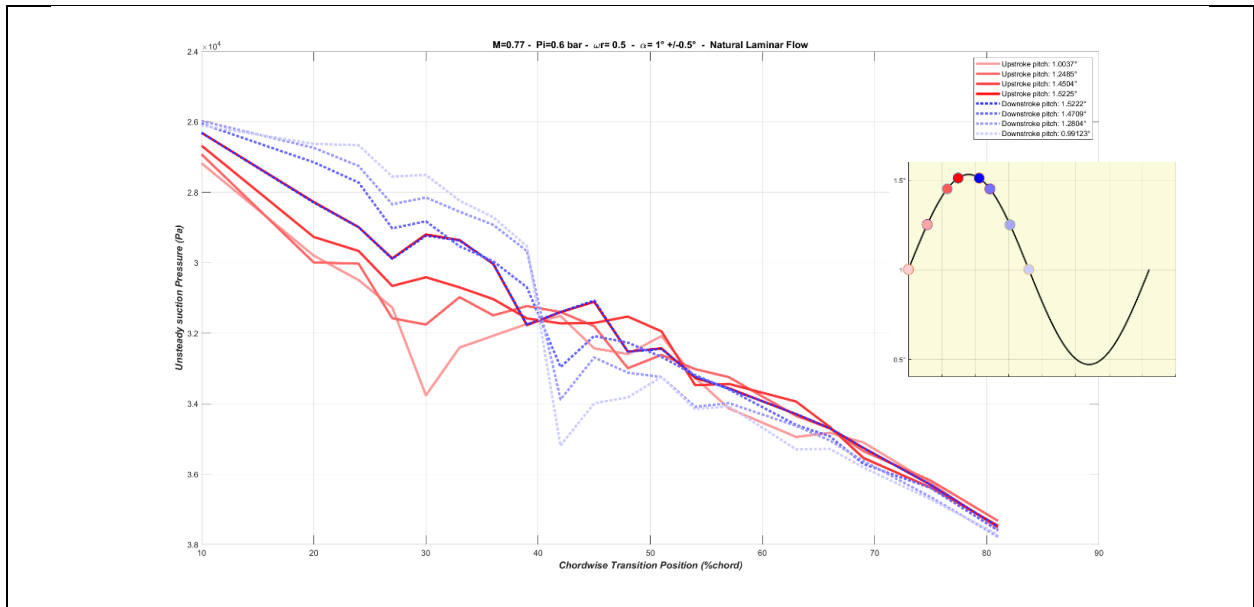

Figure 31: Snapshot at different times of the upper section unsteady pressure distribution during a pitch oscillation in free transition flow. (reddish curves = upstroke times; blueish curves =downstroke times). M=0.77 ;ωr=0.5 ; pitch =1°±0.5°

5   CONCLUSIONS

One mandatory step on the road to the aeroelastic analysis of laminar wings is the capability to understand the impact of the free boundary transition of such wings under forced harmonic motions on the unsteady aerodynamics and hence to predict accurately these latter.

To this end, an experimental campaign was conducted in the S2MA Onera's transonic wind tunnel on a laminar symmetrical 2D airfoil with fixed incidences and forced dynamic pitch oscillations in subsonic and transonic flow conditions.

Steady and unsteady measurements were carried out on this highly instrumented model using optical equipment to monitor the displacements, pressure sensors to infer the steady and unsteady loads and calibrated hot films to detect and follow the transition motion.

In steady conditions, the lift polars curve presents two linear regimes with a slope change occurring at the apparition shock incidence. These dual linear regimes are found out not only in the case of free transition but also for the triggered transition one. The transition gets attached to the shock as soon as this latter is arising, with the presence of a boundary layer separation located at the shock foot.

The pitch oscillations induce unsteady loads exhibiting hysteresis loops which remain nonetheless linear and centered on the linear steady curves. The transition chordwise travel with the harmonic pitch variations is more or less driven by the steady conditions albeit showing phase shifts between upstroke and downstroke motions, akin to the corresponding shock motions; which in turn generate also dynamic single or dual loops.

The stability analysis based on the variation of the aerodynamic derivatives with the oscillating frequency did not bring out any resonance phenomena but rather a linear behaviour more visible at high frequencies.

Lastly, (U)RANS simulations performed using a transition model based on the AHD criteria and the Spalart-Allmaras turbulence model reproduced well the experimental results.

REFERENCES

[1] Tichy L., Mai H., Fehrs M, Nitzsche J. and Hebler A. (2017). "*Risk analysis for flutter of laminar wings*", IFASD Como Italy, June 2017

[2] Mai H., Hebler A. (2011), "Aeroelasticity of a Laminar Wing", IFASD Paris June 2011

[3] Hebler A., Schojda L., Mai H. (2013), "Experimental Investigations of the Aeroelastic Behavior of a Laminar airfoil in transonic flow", IFASD Bristol GB, June 24-27 2013.

[4] Hebler A. (2017) "Experimental Assessment of the Flutter Stability of a Laminar Airfoil in Transonic Flow", IFASD 2017 Como Italy, 25-28 June 2017

[5] Braune M., Hebler A. (2018). "Experimental Investigation of Transonic Flow Effects on a Laminar Airfoil Leading to Limit Cycle Oscillations", AIAA Aviation Forum, 2018 Applied Aerodynamics Conference, Atlanta, Georgia USA, 25-29 June 2018

[6] Braune M., Hebler A. (2019), "Mechanisms of Transonic Single Degree of Freedom Flutter of a Laminar Airfoil", IFASD 2019 Savannah Georgia USA, 9-13 June 2019

[7] Mai H., Hebler A., Koch S. (2019). « High Reynolds Number Testing of a Laminar Airfoil under Forced Harmonic Pitching Oscillations at Cryogenic Conditions », IFASD 2019 Savannah Georgia USA, 9-13 June 2019

[8] Lepage A., Amosse Y., Brazier J-P., Forte M., Vermeersch O., Liauzun C. (2019). « Experimental investigation of the laminar-turbulent transition and crossflow instability of an oscillating airfoil in low speed flow », IFASD 2019, June 2019, Savannah, USA

[9] Poirel D., Harris Y., Benaissa A. (2008). « Self-sustained aeroelastic oscillations of a NACA0012 airfoil at low-to-moderate Reynolds numbers », Journal of Fluids and Structures, 24, pp 700-719

[10] Poirel D. and Mendes F. (2014), "Experimental Small-Amplitude Self-Sustained Pitch-Heave Oscillations at Transitional Reynolds Numbers", AIAA Journal, Vol. 52 No. 8

[11] Girodroux Lavigne P., Dugeai A., Sens A.S., Krueger W.R., Dimitrov D., Nitzsche J., Ritter M. and Stickan B. (2013), "*Investigations of Transonic Aircraft in the Joint DLR/ONERA Project "Non-Linear Aeroelastic Simulation, NLAS II"* ", IFASD Bristol GB, June 24-27 2013.

[12] Liauzun C. (2010), "*Aeroelastic response to gust using CFD techniques*", Proceedings of 3rd Joint US-European Fluids Engineering Summer Meeting and 8th International Conference on Nanochannels, Microchannels and Minichannels, FEDSM2010-ICNMM2010, Montreal, Canada, August 2-4 2010.

[13] Heinrich R. and Reimer L. (2013), "*Comparison of different approaches for gust modelling in the CFD code TAU*", IFASD Bristol GB, June 24-27 2013.

[14] Bekemeyer P., Thormann R. and Timme S. (2017), "*Rapid Gust Response Simulation of Large Civil Aircraft using Computational Fluid Dynamics*", The Aeronautical Journal Volume 121, issue 1246, pp1795-1807, December 2017

[15] Huvelin F., Dequand S., Lepage A. and Liauzun C. (2018), « *On the validation and use of high fidelity numerical simulations for gust response analysis* », AerospaceLab Journal issue 14, http://www.aerospacelab-journal.org

[16] Grisval J-P, Liauzun C. (1999). « *Application of the finite element method to aeroelasticity* », Revue Européenne des Eléments Finis, Vol 8, Issues 5-6, pp 553-579

[17] Garrigues E. (2018), "*A review of industrial aeroelasticity practices at Dassault Aviation for military aircraft and business jets*", AerospaceLab Journal issue 14, http://www.aerospacelab-journal.org

[18] Hue D., Vermeersch O., Bailly D., Brunet V. and Forte M. (2015). "*Experimental and Numerical Methods for Transition and Drag Predictions of Laminar Airfoils*", AIAA Journal Vol. 53 No. 9, pp2694-2712

[19] Dunham J. (1972). "*Prediction of Boundary Layer Transition on Turbomachinery Blades*", AGARD Meeting Boundary Layer in Turbomachines, Paris

[20] Abu-Ghannam B.J., Shaw R. (1980). "*Natural Transition of Boundary Layers. The effects of Turbulence, Pressure Gradient, and Flow History*", J. Mech. Engr. Science, 22(5): 213-228

[21] Drela M., Giles M.B. (1987). "*Viscous-Inviscid Analysis of Transonic and Low Reynolds Number Airfoils*", AIAA Journal, 25(10): 1347-1355

[22] Arnal D. (1989). "*Transition prediction in transonic flow,*" Symposium Transsonicum III, Springer, pp. 253–262.

[23] Perraud J., Durant A. (2016). "*Stability-Based Mach Zero to Four Longitudinal Transition Prediction Criterion,*" Journal of Spacecraft and Rockets, 2016, pp. 730–742.

[24] Gleyzes C., Cousteix J., Bonnet J-L. (1985). '*Theoretical and experimental study of low Reynolds number transitional separation bubbles*', in Conference on Low Reynolds Number Airfoil Aerodynamics, Notre Dame, IN, pp. 137–152.

[25] W. B. Roberts W. B. (1980). '*Calculation of Laminar Separation Bubbles and Their Effect on Airfoil Performance*', AIAA Journal, vol. 18, no. 1, pp. 25–31.

[26] Arnal, D., Habiballah, M., and Coustols, E. (1984). "*Théorie de l'instabilité laminaire et critères de transition en écoulement bi et tridimensionnel,*" La Recherche Aérospatiale, Vol. 2, pp. 125–143.

[27] Cakmakcioglu S. C., Bas O. and Kaynak U. (2017), "*A correlation-based algebraic transition model*", Proceedings of the Institution of Mechanical Engineers, Part C: Journal of Mechanical Engineering Science

[28] Langtry R. B., Menter F. R. (2009). "*Correlation-Based Transition Modeling for Unstructured Parallelized Computational Fluid Dynamics Codes*", AIAA Journal Vol. 47, No. 12

[29] Fehrs M. (2018). "One-Equation Transition Model for Airfoil and Wing Aerodynamics", New Results in Numerical and Experimental Fluid Mechanics XI, 136, pp199-208 Springer

[30] Pascal L., Delattre G., Deniau H., Cliquet J. (2020). « Stability-Based Transition Model Using Transport Equations », AIAA Journal, Vol 58, No 7.

[31] Stroer P., Krimmelbein N., Krumbein A., Grabe C. (2020). "Stability-Based Transition Transport Modeling for Unstructured Computational Fluid Dynamics Including Convection Effects", AIAA Journal, Vol. 58, No 4

[32] Bragin N. N., Bolsunovsky A. L., Buzoverya N. P., Puschin N. A., Skomorokhov S. I., Chernyshev I. L. (2020). "About the Flow Aerodynamic Model with engines Over the Wing", ICMAR 2020, AIP Conf. Proc. 2351, 030029-1-030029-10

[33] Fehrs M. (2013). "Influence of transitional flows at transonic Mach numbers on the flutter speed of a laminar airfoil", IFASD Bristol GB, June 24-27 2013

[34] Fehrs M., Van Rooij A.C.L.M., Nitzsche J. (2015). "Influence of boundary layer transition on the flutter behavior of a supercritical airfoil", CEAS Aeronautical Journal 6:291-303

[35] Fehrs M., Nitzsche J., Hebler A. (2017). "CFD-based flutter prediction for high Reynolds number flows with free boundary layer transition", IFASD2017, 25-28 June Como Italy

[36] Fehrs M., Helm S., Kaiser C. (2019). "Numerical investigation of unsteady transitional boundary layer flows", IFASD2019, 9-13 June 2019, Savannah, Georgia USA.

[37] Barnes C., Visbal M.R. (2020). "Transonic Effects on a Laminar Airfoil in Small-Amplitude Pitch Oscillation", AIAA Aviation 2020 Forum.

[38] Kuzmina S., Ishmuratov F., Karas O. (2019). "Some aspects of transonic flutter of aircraft with laminar wings", 8th European Conference for Aeronautics and Space Sciences (EUCASS)

[39] Liauzun C., Mortchéléwicz G. D., Lepage A (2019)., "Assessment of CFD Methods Taking into account Laminar-Turbulent Transition for Aeroelasticity of Laminar Wings", IFASD2019, Savannah Georgia USA, 9-13 June 2019

[40] Cambier L., Heib S. and Plot S. (2013), "*The Onera CFD software: input from research and feedback from industry*", Mechanics & Industry, 14, pp159-174

[41] Le Balleur J.C. (1981). "*Strong matching method for computing transonic viscous flows including wakes and separations. Lifting Airfoils.*", La Recherche Aérospatiale, 3,March, pp. 21–45.

[42] Methel J., Mery F., Vermeersch O., Forte M., Delattre G., Rouvière A., (2023), "Laminar turbulent transition experiment on the effect of surface imperfections on an NLF airfoil in transonic flow" https://doi.org/10.21203/rs.3.rs-2591458/v1

[43] Drela M., Giles M. B. (1987), "ISES: A Two-Dimensional Viscous Aerodynamic Design and Analysis Code", 25th AIAA Aerospace Sciences Meeting march 1987, Reno NV USA

COPYRIGHT STATEMENT